C O M M O N S D E E D

저작자표시 **2.0** 대한민국

이용자는 아래의 조건을 따르는 경우에 한하여 자유롭게

- 이 저작물을 복제, 배포, 전송, 전시, 공연 및 방송할 수 있습니다.
- 이차적 저작물을 작성할 수 있습니다.
- 이 저작물을 영리 목적으로 이용할 수 있습니다.

다음과 같은 조건을 따라야 합니다:

저작자표시. 귀하는 원저작자를 표시하여야 합니다.

- 귀하는, 이 저작물의 재이용이나 배포의 경우, 이 저작물에 적용된 이용허락조건을 명확하게 나타내어야 합니다.
- 저작권자로부터 별도의 허가를 받으면 이러한 조건들은 적용되지 않습니다.

저작권법에 따른 이용자의 권리는 위의 내용에 의하여 영향을 받지 않습니다.

이것은 이용허락규약(Legal Code)을 이해하기 쉽게 요약한 것입니다.

Disclaimer

공학박사 학위논문

Investigation of Deuterium Plasma Property Variation by Carbon Impurity from Graphite

흑연으로부터의 탄소 불순물 유입에 의한 중수소 플라즈마 특성 변화 연구

2015년 2월

서울대학교 대학원
에너지시스템공학부 원자핵공학전공
임 선 택

Investigation of Deuterium Plasma Property Variation by Carbon Impurity from Graphite

흑연으로부터의 탄소 불순물 유입에 의한 중수소 플라즈마 특성 변화 연구

지도교수 김 곤 호

이 논문을 공학박사학위논문으로 제출함
2014년 10월

서울대학교 대학원
에너지시스템공학부 원자핵공학전공
임 선 택

임선택의 박사학위논문을 인준함
2014년 12월

위 원 장	박 종 래	(인)
부위원장	김 곤 호	(인)
위 원	유 세 기	(인)
위 원	정 구 환	(인)
위 원	홍 석 호	(인)

Abstract

Investigation of Deuterium Plasma Property Variation by Carbon Impurity from Graphite

Lim Sun-taek
Department of Energy Systems Engineering
The Graduate School
Seoul National University

Spatially and temporally varying deuterium plasma properties caused by carbon impurity influx are investigated on the basis of morphological change of graphite that has strong influences on the formation of carbon impurities. The present study aims to provide a new perspective on interpreting plasma-surface interactions by considering the surface morphological change. It is revealed that the consideration of the variations of both the plasma property and the graphite morphology is necessary to understand the deuterium plasma - graphite surface interaction. Electron cyclotron resonance (ECR) plasma was used to graphite target as the main interaction area and to accelerate ions with

vertical incidence on the target. Experiments were carried out with a plasma density range of 1 - 3.5 × 10^{11} cm^{-3}, an electron temperature range of 3.5 - 5.5 eV, and an ion energy range of 17 - 100 eV, which are experimental conditions similar for the KSTAR scrape-off layer (SOL) plasma.

The morphological change of the graphite caused by deuterium plasma irradiation was analyzed according to the energy dose, which is the product of the energy and dose of ions, and therefore the energy dose indicates the total energy transferred on graphite per unit area. The energy dose determines the degree of the morphological change of the graphite as the energy needed for motion of carbon atoms causing the morphological change is proportional to the energy dose. Moreover, energetic deuterium ion actively reacts and bonds with the carbon, resulting in the C-D bond formation on the graphite surface. Accordingly, the energy dose was applied up to the KSTAR SOL plasma steady-state condition to analyze progress of the morphological change of the graphite. As a result, the graphite morphology changed from a plane surface to a conical tip as the energy dose is increased. Further increases in the energy dose enlarged the size and the aspect ratio of the conical tip. The increased sp^3 character on graphite by the ion irradiation is turned out to induce conical tip formation on the graphite surface by containing a small amount of diamond-like carbon, which has a slightly higher displacement threshold energy than graphitic atoms. The

formation of the cone-shaped carbon bundle owing to the gathering of small conical tips occurs when the sheath electric field is stronger than 3.8×10^5 V/m. Therefore, plasma physical properties such as the energy dose, sheath electric field, and plasma chemical property of C-D bond formation play crucial roles in cone-shaped carbon bundle formation. The results indicate that the interpretation of the plasma-based physics and chemistry are necessary to analyze the morphological change of graphite.

A sputtering yield model for the conical tip is established. Considering that the morphological change of the graphite surface entails the increment in the local angle of ion incidence and the additional collisions of backscattered ions, the Roth's model for a plane surface has been modified. The newly established sputtering yield model reflects analytical anticipation that the morphological change of graphite caused by the energy of the ions increases the physical and chemical sputtering yields compared to those for a plane surface. The measured sputtering yields for the morphologically changed graphite surface indeed turned out to be two times larger than those estimated using Roth's model for a plane surface owing to the morphological change of graphite. The results indicate that the interpretation of the plasma physics is necessary to analyze both the morphological change of graphite and the carbon impurity formation.

The inflow of deuterated carbon decreases the electron temperature and increases the electron density in space, as the deuterated carbon is more likely to be dissociated or ionized as a result of collisions with electrons than those for deuterium. The spatial variation of deuterium plasma properties was experimentally analyzed by based on a global model that calculates the spatially averaged plasma properties. It is found that increase in the sputtering yield slightly raises a few % of the ratio of deuterated carbon to deuterium plasma, and this slight increment induces the variation of the deuterium plasma properties. The results indicate that the interpretation of the interaction between the carbon impurity and the deuterium plasma is necessary to analyze the deuterium plasma properties.

The inflow of deuterated carbon decreases the electron temperature and increases the electron density with time, because the morphological change of graphite with the operation time increases the sputtering yield. Increases in the ion energy and ion flux, i.e., an increase in the energy dose, cause a severe morphological change of graphite, resulting in large variations of the deuterium plasma properties. In addition, the increased ion flux due to the carbon impurity influx into the deuterium plasma causes additional collisions of backscattered ions, resulting in the re-increment of the sputtering yield. Therefore, it is discovered that the variation of the deuterium plasma properties caused by the carbon impurity influx can accelerate graphite wall erosion.

In this study, plasma and graphite are analyzed simultaneously in order to examine the interaction between the deuterium plasma and the graphite surface. The morphological change of graphite, in particular, is found to be a major factor to be considered in deuterium plasma - graphite surface interaction. The morphological change of the graphite caused by deuterium plasma irradiation increases the carbon impurity influx into the deuterium plasma, resulting in large variations of the deuterium plasma properties. New discoveries described in this study will greatly contribute to understanding of the KSTAR plasma, which uses deuterium plasma with graphite, and the plasma processing for carbon and hydrogen gases. Moreover, revealed that the variation of the plasma properties according to the operation time can be caused by the by-products, this study is believed to provide important basis for the estimation and control of plasma properties in the related fields of study.

Keywords : Deuterium plasma - graphite surface interaction, Morphological change of graphite, Sputtering yield, Carbon impurity influx, Variation of plasma properties

Student Number : 2010-30257

Contents

Abstract i
Contents vi
List of Figures ix
List of Tables xviii

Chapter 1. Introduction 1
1.1. Motivation 1
1.2. Previous Studies on Interaction between Deuterium Plasma and Graphite Surface 5
1.2.1. Interaction between Deuterium Plasma and Graphite Surface 5
1.2.2. Sputtering Yield of Graphite 9
1.3. Objective and Scope of This Study 12

Chapter 2. Experimental Setup 16
2.1. ECR Plasma Source for High Density Ion Irradiation 16
2.2. Determination of Ion Irradiation Conditions for DC Biased Target 22
2.3. Determination of Ion Irradiation Conditions for Pulse Biased Target 25

Chapter 3. Increment of Carbon Impurity Formation by Morphological Change of Graphite 29

3.1. Energy Dose for Morphological Change of Graphite Irradiated by Deuterium Plasma 29

3.2. Morphological Change of Graphite by Deuterium Plasma Irradiation 32

3.2.1. Morphological Change of Graphite with Energy Dose 32

3.2.2. Formation Mechanism of Conical Tips on Graphite 36

3.2.3. Formation Mechanism of Cone-shaped Carbon Bundle on Graphite 43

3.3. Increment of Sputtering Yield by Morphological Change of Graphite 57

3.3.1. Sputtering Yield Model with Consideration of Graphite Morphology 57

3.3.2. Increment of Sputtering Yield by Morphological Change of Graphite 65

Chapter 4. Variation of Deuterium Plasma Properties by Carbon Impurity 71

4.1. Global Model for Spatially Averaged Deuterium Plasma Properties 71

4.2. Spatially Varying Deuterium Plasma Properties by Carbon Impurity 81
4.2.1. Decrease of Electron Temperature and Increase of Electron Density in Space 81
4.2.2. Bulk Plasma Variation by Increased Carbon Impurity Influx 85
4.3. Temporally Varying Deuterium Plasma Properties by Carbon Impurity 89
4.3.1. Decrease of Electron Temperature and Increase of Electron Density with Operation Time 89
4.3.2. Intensified Variation of Plasma Properties by Graphite Morphology 94

Chapter 5. Re-Increment Mechanism of Carbon Impurity Formation by Increase of Ion Flux 96

Chapter 6. Conclusions 102

References 105

초록 111

List of Figures

Figure 1.1.	(a) Measured electron temperature (square with solid line) and electron density (circle with dotted line) with distance from the target in an ECR chamber at an ion energy of 100 eV and microwave power of 400 W. Empty symbol: stainless steel target; filled symbol: graphite target. (b) Measured electron temperature (square with solid line) and electron density (circle with dotted line) with operation time in an ECR chamber at an ion energy of 100 eV. Empty symbol: microwave power of 400 W; filled symbol: microwave power of 600 W.	4
Figure 1.2.	Schematics of point of view on the deuterium plasma and graphite surface interaction in (a) previous study and (b) this study.	14
Figure 2.1.	Schematic diagram of an ECR chamber for deuterium ion irradiation of graphite.	19
Figure 2.2.	Magnetic field distribution with the distance from graphite target in an ECR chamber at a coil current of 110 A.	20
Figure 2.3.	The variation of the surface temperature for an incident ion energy range of 17 - 100 eV in an ECR chamber.	20

Figure 2.4.	(a) Plasma potential, (b) electron temperature (filled squire with solid line) and electron density (empty circle with dotted line) in an ECR chamber at a deuterium pressure of 1 mTorr, a coil current of 110 A, microwave of 400 W.	24
Figure 2.5.	The variation of the sheath electric field with the target bias potential, as calculated with equation (2.3).	27
Figure 2.6.	The variations of the target bias potential with pulse period on the target for various pulse bias voltages show the rapid pulse rise and slow fall time. The pulse system was operated for a duration of 100 ms (10 Hz) with a pulse length on load in the range 130 to 200 μs.	28
Figure 3.1.	SEM images of graphite samples after ion irradiation with (a) an ion energy of 40 eV and an ion dose of 9.5×10^{20} cm^{-2}, and (b) an ion energy of 70 eV and an ion dose of 4.8×10^{20} cm^{-2}. Energy doses are (a) 60.8 MJ/m^2 and (b) 53.8 MJ/m^2.	31
Figure 3.2.	(a) Nanoscale conical tip formation at the energy dose of 0.32 MJ/m^2. (b) Conical tip formation at the energy dose of 76.8 MJ/m^2. (c) Cone-shaped carbon bundle formation at the energy dose of 152 MJ/m^2. (d) Conical tip with eroded surface at the energy dose of 5108 MJ/m^2. (e) Conical tip with eroded surface at the energy dose of 9000 MJ/m^2.	34

Figure 3.3.	Morphological change of graphite with the energy dose.	35
Figure 3.4.	SEM images of graphite (a) before and (b)-(d) after ion irradiation at a dose of 5×10^{16} cm^{-2}. Sheath electric fields are (b) 3.37×10^5 V/m, (c) 3.83×10^5 V/m, and (d) 4.55×10^5 V/m.	38
Figure 3.5.	Raman spectra of pristine (before irradiation) and ion irradiated graphite; an ion dose was 5×10^{16} cm^{-2}.	39
Figure 3.6.	SEM images of graphite samples after ion irradiation with a sheath electric field of 4.55×10^5 V/m and various ion doses: (a) 1×10^{16} cm^{-2}, (b) 5×10^{16} cm^{-2}, (c) 1×10^{17} cm^{-2}, (d) 2×10^{17} cm^{-2}, and (e) 5×10^{17} cm^{-2}. (f) The variation in the size of the conical tips with a dose of ions.	41
Figure 3.7.	Raman spectra of pristine graphite (before irradiation) and ion irradiated graphite irradiated with a sheath electric field of 4.55×10^5 V/m and various ion doses: 1×10^{16} cm^{-2}, 5×10^{16} cm^{-2}, 1×10^{17} cm^{-2}, 2×10^{17} cm^{-2}, and 5×10^{17} cm^{-2}.	42

Figure 3.8. Thirty degrees tilted SEM images of graphite after ion irradiation at constant ion flux of 1.8×10^{17} $cm^{-2}s^{-1}$. The ion irradiation conditions are (a) an ion energy of 40 eV, a sheath electric field of 3×10^{5} V/m, and an ion dose of 4.8×10^{20} cm^{-2}, (b) an ion energy of 40 eV, a sheath electric field of 3×10^{5} V/m, and an ion dose of 9.5×10^{20} cm^{-2}, (c) an ion energy of 100 eV, a sheath electric field of 3.8×10^{5} V/m, and an ion dose of 4.8×10^{20} cm^{-2}, and (d) an ion energy of 100 eV, a sheath electric field of 3.8×10^{5} V/m, and an ion dose of 9.5×10^{20} cm^{-2}. 45

Figure 3.9. Top (a, c, e) and thirty degrees tilted SEM images (b, d, f) of graphite after ion irradiation at constant ion energy of 100 eV, an ion flux of 2.8×10^{17} $cm^{-2}s^{-1}$, and a sheath electric field of 4.9×10^{5} V/m. Doses of ions are (a), (b) 9.5×10^{20} cm^{-2}, (c), (d) 1.9×10^{21} cm^{-2}, and (e), (f) 3.8×10^{21} cm^{-2}. 47

Figure 3.10. Top-view SEM images of graphite after ion irradiation at constant ion energy of 100 eV. Sheath electric fields are (a) 1.4×10^{5} V/m at an ion dose of 2.3×10^{20} cm^{-2}, (b) 3.0×10^{5} V/m at an ion dose of 9.5×10^{20} cm^{-2}, and (c) 4.9×10^{5} V/m at an ion dose of 9.5×10^{20} cm^{-2}. 49

Figure 3.11. Schematic diagram of the cone-shaped carbon bundle formation on the graphite: (a) formation of nanoscale dot-like structures by ion incidence or deposition of impurity atom from sample holder/inner wall of chamber act as a precursor; (b) initial conical tip formation is generated due to difference of sputtering yields; (c) conical tips with greater height are generated by increases in an ion dose; and (d) the cone-shaped carbon bundle formation through the collection and welding of adjacent conical tips due to attractive dipole forces. 51

Figure 3.12. Schematic of the interaction between the conical tip 1 and the adjacent conical tip 2. E_{sh} is a sheath electric field, $\vec{p}$ is the induced dipole moment along the axis of the conical tip 2, F_{align} is the aligning force, F_{dipole} is the dipole force, Θ is the angle between the axis of the conical tip 2 and a sheath electric field. 54

Figure 3.13. Diameters (filled square) and heights (empty circle) of the conical tip on the graphite after ion irradiation at constant ion energy of 100 eV. Ion fluxes are (a) 1.8×10^{17} $cm^{-2}s^{-1}$ and (b) 2.8×10^{17} $cm^{-2}s^{-1}$. 58

Figure 3.14. Diameters (filled square) and heights (empty circle) of the conical tip on the graphite after ion irradiation at constant ion flux of 2.8×10^{17} $cm^{-2}s^{-1}$. Ion doses are (a) 4.8×10^{20} cm^{-2} and (b) 9.5×10^{20} cm^{-2}. 58

Figure 3.15.	Schematic illustration of the trajectory of ion incidence on the conical shaped graphite morphology. Ion is irradiated with local angle of σ due to cone angle of ϕ. Backscattered ion with form of neutral is irradiated on the neighboring cone with local angle of $\lvert \pi - 3\sigma \rvert$.	60
Figure 3.16.	(a) Projected energy range, a, and (b) energy range straggling along the longitudinal direction, a, with angle of ion incidence for an ion energy ranges of 17 - 100 eV.	61
Figure 3.17.	(a) Backscattered ion ratio, and (b) energy of backscattered ion with angle of ion incidence for an ion energy ranges of 17 - 100 eV.	62
Figure 3.18.	(a) Physical sputtering yield by incidence of initial ion, and (b) chemical sputtering yield by backscattered ion with angle of ion incidence at an ion energy ranges of 17 - 100 eV.	63
Figure 3.19.	Thirty degrees tilted SEM images of graphite (a) before and (b)-(e) after ion irradiation at a constant ion flux of 2.7×10^{17} $cm^{-2}s^{-1}$ and a dose of ion is 9.5×10^{20} cm^{-2}. Ion energies are (b) 17 eV, (c) 40 eV, (d) 70 eV, and (e) 100 eV.	67

Figure 3.20. (a) Physical and (b) chemical sputtering yields of graphite with an ion energy range of 17 – 100 eV. Plane surface model (Roth) represents the sputtering yield for plane surface and modified model represents the sputtering yield for conical tip. 68
Figure 3.21. Total sputtering yields of graphite with an ion energy range of 17 – 100 eV. Plane surface model (Roth) represents the sputtering yield for plane surface, modified model represents the sputtering yield for conical tip, and measurement represents the sputtering yield by weight loss method. 70
Figure 4.1. Computed neutral densities of deuterium and deuterated carbon species by the global model with microwave power of 400 W and an ion energy of 40 eV. 79
Figure 4.2. Partial pressure of deuterated methane (CD_4) with operation time for an incident ion energy range of 17 – 100 eV in an ECR chamber. A deuterium gas pressure of 1 mTorr and microwave power of 400 W are maintained in the whole operation time. 80
Figure 4.3. Measured electron temperature (square with solid line) and electron density (circle with dotted line) with distance from the target in an ECR chamber at an ion energy of 100 eV and microwave power of 400 W. Empty symbol: stainless steel target; filled symbol: graphite target. Ion energies are (a) 17 eV and (b) 40 eV. 83

Figure 4.4. Rate coefficients of dissociation and ionization of deuterated methane (CD_4) and deuterium (D_2). 84

Figure 4.5. (a) Measured electron temperatures and (b) electron densities for a graphite target which are normalized by those for a stainless steel target in an ECR chamber at microwave power of 400 W. 86

Figure 4.6. Computed and measured electron temperatures (square with solid line) and electron densities (circle with dotted line) with sputtering yield at an ion energy of 40 eV. Empty symbol: computed values; filled symbol: measured values. Measured values are positioned at sputtering yields of 0 and 0.029 for a stainless steel target and a graphite target, respectively. 88

Figure 4.7. (a) Measured electron temperature (square with solid line) and electron density (circle with dotted line) with operation time in an ECR chamber at an ion energy of 40 eV. Empty symbol: stainless steel target; filled symbol: graphite target. (b) Computed and measured electron temperatures (square with solid line) and electron densities (circle with dotted line) with sputtering yield at an ion energy of 40 eV. Empty symbol: computed values; filled symbol: measured values. Measured values are positioned at sputtering yields of 0 and 0.029 for operation times of 0 and 1800 sec, respectively. 91

Figure 4.8. Measured electron temperature (square with solid line) and electron density (circle with dotted line) with operation time in an ECR chamber at an ion energy of 100 eV. Empty symbol: microwave power of 400 W; filled symbol: microwave power of 600 W 93

Figure 4.9. Electron density which is divided by electron density at operation time of 0 min with operation time in an ECR chamber at ion energies of 40 and 100 eV and microwave powers of 400 and 600 W. 95

Figure 5.1. (a) Ion flux and (b) surface temperature of graphite with operation time for microwave powers of 400 and 600 W at constant coil current of 110 A and an ion energy of 100 eV. 97

Figure 5.2. Thirty degrees tilted SEM images of graphite after ion irradiation at a constant ion energy of 100 eV. Microwave powers of (a) 400 W and (b) 600 W. 99

Figure 5.3. (a) The product of backscattered ion ratio and chemical sputtering yield by incidence of backscattered ion, and (b) total sputtering yield with operation time at constant coil current of 110 A, ion energy of 100 eV, and microwave powers of 400 W and 600 W. 100

Figure 5.4. Total sputtering yields of graphite with an ion energy of 100 eV. Roth model represents the sputtering yield for plane surface and modified model represents the sputtering yield for conical tip. 101

List of Tables

Table 3.1.	Physical, chemical and total sputtering yields of graphite in eq. (3.13) from Roth model for plane surface and modified model for conical shaped surface with an ion energy range of 17 – 100 eV at a constant ion flux of 2.7×10^{17} $cm^{-2}s^{-1}$.	68
Table 4.1.	Ion species, neutral species and sticking coefficients [44] in the global model.	72
Table 4.2.	Electron reactions with atoms and molecules. Rate coefficients are used in Ref. [44-51].	73
Table 4.3.	Neutral – neutral reactions. Rate coefficients are used in Ref. [44, 52-55] and T is the gas temperature.	74
Table 4.4.	Ion – neutral reactions. Rate coefficients are used in Ref. [44, 55-58].	75

Chapter 1. Introduction

1.1. Motivation

The deuterium plasma–graphite surface interaction has been widely investigated as graphite has been one of the common materials used for the plasma-facing component (PFC) in fusion devices [1–4]. However, in previous studies of the deuterium plasma–graphite surface interaction, the effect of the morphological change of graphite on the deuterium plasma properties was not investigated. Although the morphological change of graphite is determined by the irradiated deuterium plasma, properties of deuterium plasma during its irradiation on morphologically changed graphite were not discussed, which might be due to the absence of established relationship between the deuterium plasma and graphite surface. In order to investigate on this relationship, the major factors that govern the linkage between the deuterium plasma and graphite surface were thoroughly examined.

In order to discover a key factor that links between the deuterium plasma and graphite surface, a comparative analysis of graphite and stainless steel under the same plasma treatment condition has been carried out (Fig. 1.1). Figure 1.1(a) shows the measured electron temperature and electron density for a

stainless steel and a graphite in an electron cyclotron resonance (ECR) chamber at an ion energy of 17 eV and microwave power of 400 W. Up to 60 mm from the target, the electron temperature for a graphite target was lower than that for a stainless steel target, and the electron density for a graphite target was higher than that for a stainless steel target. Because the operation conditions such as deuterium pressure, coil current, microwave power, and ion energy are constant, different types of targets cause spatial variation of deuterium plasma properties. Figure 1.1(b) shows the measured electron temperature and electron density according to operation time in an ECR chamber at an ion energy of 100 eV. The microwave powers are 400 W for an average ion flux of 1.8×10^{17} $cm^{-2}s^{-1}$ and 600 W for an average ion flux of 2.8×10^{17} $cm^{-2}s^{-1}$. The decrease in electron temperature and the increase in electron density are observed, and then both stabilize, demonstrating temporal variation of deuterium properties during its irradiation on a graphite. Considering that the carbon impurity (C_xD_y), which is the by-product of the reaction between the deuterium plasma and graphite, is not generated by the plasma irradiation on a stainless steel, carbon impurity can cause the variation of the deuterium plasma properties according to time. Therefore, in this study, the carbon impurity is considered as a key factor that links between the deuterium plasma and graphite, and the variation of the deuterium plasma properties during its irradiation on graphite is

analyzed based on the levels of carbon impurity. In particular, this study considers the effect of the morphological change of graphite on the increment of carbon impurity formation, which was not considered in previous studies related to the deuterium plasma‐graphite surface interaction. The present study aims to provide a new perspective on interpreting plasma-surface interactions by considering the surface morphological change.

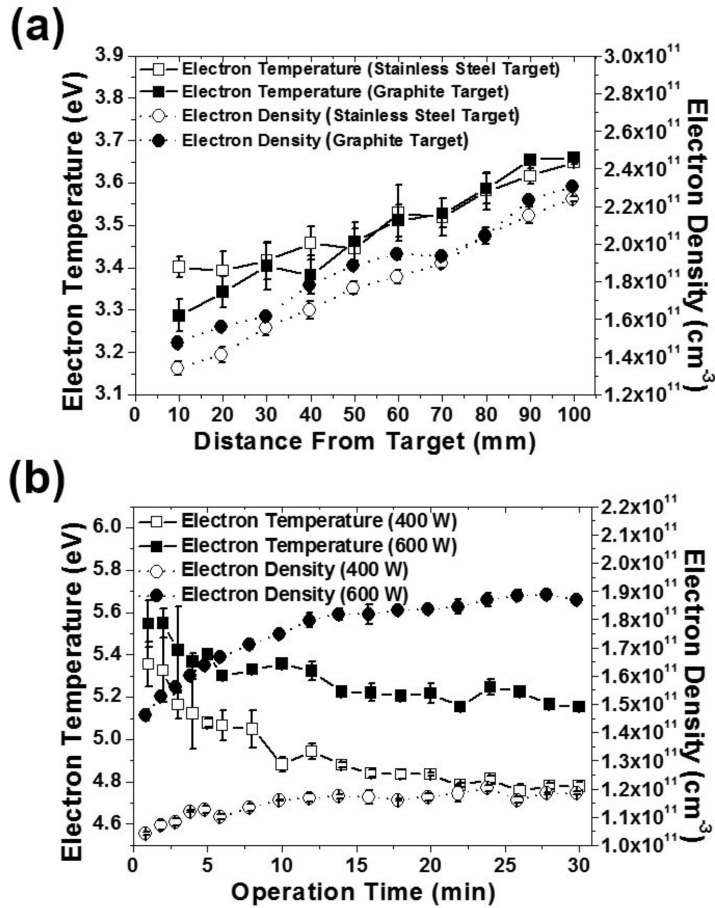

Figure. 1.1. (a) Measured electron temperature (square with solid line) and electron density (circle with dotted line) with distance from the target in an ECR chamber at an ion energy of 100 eV and microwave power of 400 W. Empty symbol: stainless steel target; filled symbol: graphite target. (b) Measured electron temperature (square with solid line) and electron density (circle with dotted line) with operation time in an ECR chamber at an ion energy of 100 eV. Empty symbol: microwave power of 400 W; filled symbol: microwave power of 600 W.

1.2. Previous Studies on Interaction between Deuterium Plasma and Graphite Surface

1.2.1. Interaction between Deuterium Plasma and Graphite Surface

Because deuterium, rather than hydrogen, is used in fusion plasma [1 - 4], the deuterium plasma - graphite surface interaction has been widely studied. Until the year 2000, studies focused on atomic-scale interactions [5 - 7]. The irradiated deuterium ion causes physical and chemical sputtering, resulting in the formation of carbon (C) and deuterated carbon (CD_4), respectively. The physical and chemical sputtering yields for the plane surface were well defined by Roth [8]. Sputtered carbon has a strong affinity for the surrounding deuterium ions and redeposits to form a deuterium-rich amorphous carbon layer on the graphite surface. The modeling of the interaction between the deuterium plasma and the redeposited amorphous carbon layer [6], as well as the motion of an impurity particle through the plasma [7], was performed. Here, the deuterium plasma conditions were used as the initial and boundary conditions. For example, background plasma was used as an input condition in the ERO code modeling of the motion of the impurity particle through the plasma [7]. After the year 2000, it was considered that plasma

properties are changed by the interaction between the plasma and impurities [9, 10]. The effects of impurities on the deuterium plasma, such as radiative cooling [9], were considered, and the effect of the dust on the deuterium plasma properties was considered [10]. Currently, plasma properties, especially the plasma flux on the target, are controlled using an intentionally seeded impurity [11–13]. In summary, a carbon impurity can cause the spatially and temporally varying deuterium plasma properties. However, previous studies of the deuterium plasma–graphite surface interaction considered only the plane surface, without considering the morphological change of the graphite, despite the observation of morphological changes such as conical tips [14, 15], cracks [16], and surface erosion [17] in various experiments.

The formation of conical tips is a typical change in the surface morphology of a graphite target facing deuterium plasma ion irradiation. Balden et al. [14] performed a study using planar inductively coupled plasma (ICP) with deuterium ion energy of 30 eV and a flux of 3×10^{17} $cm^{-2}s^{-1}$. They observed the formation of conical tips with sizes of a few tens of nanometers on graphite when the total dose was 6.8×10^{21} cm^{-2} at 500 K. Baldwin et al. [15] observed that the size of the tips increased with a dose of ions. In the PISCES-B experiment, a graphite target was exposed to deuterium ion energy of 40 eV and a flux of 6×10^{18} $cm^{-2}s^{-1}$, and conical tips with sizes of a few hundred

nanometers formed on the graphite when the total dose was 2 × 10^{22} cm^{-2} at 600 K. Furthermore, in a study using the ICP source, Balden observed the effects of simultaneous thermal (atomic) and energetic (ionic) deuterium impact on morphological changes in graphite and compared them to ion beam bombardment results. The pure and Ti-doped graphites bombarded with an ion beam had needle-like structures. This implies that the directional impact of the energetic ions enhances the depth of the sputter etch, which is one of the dominant physical reaction processes in these systems. In pure and Zr-doped graphites exposed to plasma, the directional structure is smeared, and instead, conical tips are observed. These results reveal that the energy and dose of the irradiation ions play important roles in the formation of conical tips on the graphite. In addition, cracks are generated by the surface chemical erosion mechanism, as discussed in our previous study [16]. Yang et al. [16] performed a study using ECR plasma with hydrogen ion energy of 100 eV and a flux of 6.4 × 10^{16} $cm^{-2}s^{-1}$. They observed the uniform cracking of the surface of the irradiated graphite by the decomposition of the less-ordered carbonaceous species.

The previous studies reveal that a carbon impurity can cause the spatial and temporal variation of the deuterium plasma properties. However, previous studies of the deuterium plasma–graphite surface interaction considered only the plane surface, without consideration of the morphological change of the graphite.

Because a carbon impurity can cause the variation of the deuterium plasma properties, it is necessary to understand the effects of the morphological change of graphite on the carbon impurity formation, i.e., the sputtering yield. For example, the increment of the ion incidence angle caused by the morphological change of graphite can increase the sputtering yield [18]. This is discussed in detail in the following section.

1.2.2. Sputtering Yield of Graphite

Impurities are defined as atoms, molecules, and particles without fuel gas [19]. In this study, a carbon impurity is defined as C atoms and deuterated carbon (C_xD_y) molecules without the fuel gas of deuterium for the deuterium plasma - graphite surface interaction. The carbon impurity influx from the graphite is defined as

$$\Gamma_{impurity} = Y\Gamma_i \qquad (1.1)$$

Here, Y is the sputtering yield of the graphite, and Γ_i is the incident ion flux. The physical and chemical sputtering yields for the plane surface are well defined by Roth [8]. The total sputtering yield is expressed as

$$Y_{tot} = Y_{phys} + Y_{therm}(1 + DY_{dam}) + Y_{surf} \qquad (1.2)$$

Here, Y_{phys} is the physical sputtering yield, Y_{therm} is the thermal erosion yield, D is a parameter that depends on the hydrogen isotope, Y_{dam} is the enhanced sputtering caused by radiation damage, and Y_{surf} is the surface erosion. The second and third terms on the right-hand side of Eq. (1.2) represent the "chemical sputtering yield." The physical sputtering yield is defined by an energy of ions, and the chemical sputtering yield is defined by an energy of ions, a flux of ions, and surface temperature. When the ion has an incident angle with respect to the normal direction of the surface, the sputtering yield depends on this angle [18],

which is expressed as

$$\frac{Y(E,\theta)}{Y(E,\theta=0)}=\cos\theta\exp[2(1-\cos^2\theta)] \tag{1.3}$$

Here, E is the energy of the ion, and θ is the difference between the ion incidence angle and normal direction of the surface. When a magnetic field is present, θ is determined by the magnetic field [19]. Considering the surface roughness, the local angle of ion incidence, σ, is generated by the varied surface morphology not present in the plane surface [20]. The difference in the sputtering yields between a plane surface and a varied surface increases with the ion incidence angle [20]. Backscattered ions in a neutral form leave the surface at an ion incidence point cosine distributed [20]. Because the number of collisions by backscattered ions is determined from the local incidence angle of the ions, ion incidence on the varied surface morphology causes additional collisions of backscattered ions on the graphite surface. Thus, the sputtering yield is affected by the morphological change of the graphite due to the increase of the local angle of the ion incidence and additional collisions of backscattered ions.

The ion flux for normal incidence is expressed as

$$\Gamma_i=n_eC_s=n_e\sqrt{\frac{kT_e+kT_i}{m_i}} \tag{1.4}$$

Here, n_e is the electron density, C_s is the ion Bohm velocity, k is the Boltzmann constant, T_e is the electron temperature, T_i is the ion temperature, and m_i is the mass of an ion [19, 21]. Thus, the

ion flux is a function of the electron density, electron temperature, ion temperature, and ion mass. When CH_4 is added to the H_2 plasma, the decrease of an electron temperature and the increase of an electron density were observed with the CH_4 influx into the H_2 plasma [22]. Because the cross-sections of hydrogen isotopes are similar to each other, the interaction between the deuterium (D_2) plasma and deuterated carbon (CD_4) is similar to that between the H_2 plasma and CH_4 gas. Therefore, the ion flux is affected by the flowed carbon impurity properties. Thus, the carbon impurity influx ($\Gamma_{impurity}$) varies by the graphite morphology (Y) and flowed carbon impurity properties (Γ_i).

1.3. Objective and Scope of This Study

In previous studies of the deuterium plasma‐graphite surface interaction, the effects of the morphological change of graphite were not considered in the analysis. The ion irradiation, Γ_i^0, and carbon impurity formation, $\Gamma_{impurity}^0$, were used to be determined by the initial plasma properties and the initial state of the graphite surface, which is a plane, as shown in Fig. 1.2(a). For carbon impurities formed during deuterium ions (D^+, D_2^+) irradiation, two types were considered, carbon (C) by physical sputtering and deuterated carbon (CD_4) by chemical sputtering. However, the graphite morphology changes during the interaction and the surface no longer is the plane, which should affect process of the carbon impurity formation and properties of the plasma as well. Therefore, the effects of the morphological change of graphite on the carbon impurity formation and on plasma properties need to be considered in the study of the deuterium plasma-graphite surface interaction. Figure 1.2(b) shows a schematic that describes the interaction between deuterium plasma and morphologically changed graphite surface. The carbon impurity influx is considered as a key factor that links between the deuterium plasma and graphite. The initial ion flux, Γ_i^0, generates the initial carbon impurity influx, $\Gamma_{impurity}^0$. However, the morphological change of graphite generates the

local angle of ion incidence, σ, and additional collisions of backscattered ions, resulting in an increase in the sputtering yield and therefore changes initial value for carbon impurity influx (i.e. $\Gamma^{1}_{impurity}$). Moreover, the increased carbon impurity also changes the deuterium plasma properties, especially an electron temperature and an electron density, resulting in the variation of the ion flux, Γ^{1}_{i}, on the surface. Taking all these variations resulted from morphological change of graphite into account, the carbon impurity influx and the plasma ion flux are newly defined in this study. An attempt to understand the effects of the morphological change of graphite during deuterium plasma-graphite surface interaction is a new approach in the related fields of study. Therefore, the new discoveries described in this study will provide an unprecedented opportunities to investigate plasma-surface interactions with a new perspectives by considering the surface morphological change.

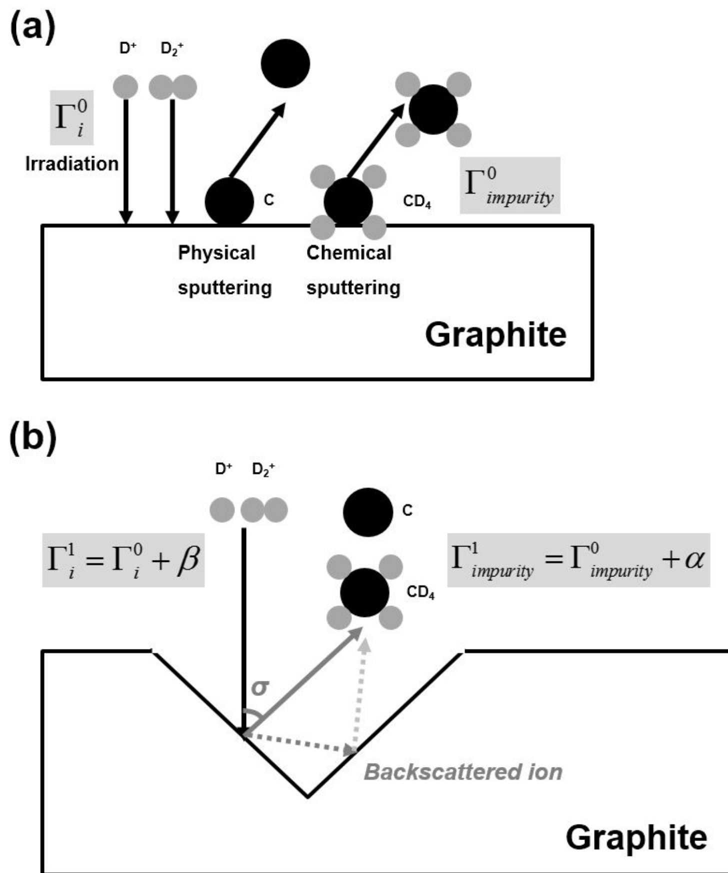

Figure. 1.2. Schematics of point of view on the deuterium plasma and graphite surface interaction in (a) previous study and (b) this study.

This study aims to determine the effect of the morphological change of graphite on the deuterium plasma - graphite surface interaction. The analysis was carried out with the following conditions: 1. Application of the monotonic energy of incident ions with a high ion flux, 2. Settings of target area to be a

graphite only, and 3. Employment of vertical incidence of ions on the target. The irradiation conditions are presented in detail in Chapter 2. In Chapter 3, the increment of the carbon impurity formation caused by the morphological change of the graphite is investigated. The morphological change of the graphite due to the deuterium plasma irradiation is analyzed by varying energy dose, in which ranges are determined by considering the material deformation and plasma conditions. A modification of the sputtering yield model based on the Roth's model which is for a plane surface is performed to reflect the increment of the sputtering yield caused by the morphological change of the graphite. In Chapter 4, the mechanism for deuterium plasma property variation caused by the carbon impurity influx is investigated. The interaction between the carbon impurity and deuterium plasma is studied both experimentally and analytically using a global model. It is revealed that the carbon impurity influx causes a decrease in electron temperature and an increase in electron density. In Chapter 5, the mechanism for re-increment of the carbon impurity by the increase of an ion flux is investigated. As a result of the interaction between the deuterium plasma and carbon impurity, it is observed that there is a synergetic effects between ion flux and the amount of carbon impurities such that carbon impurity influx increases the ion flux and increased ion flux re-increases the carbon impurities. Finally, conclusions are presented in Chapter 6.

Chapter 2. Experimental Setup

2.1. ECR Plasma Source for High Density Ion Irradiation

A schematic of an ECR plasma chamber is presented in Fig. 2.1. The reactor comprises a source chamber and a downstream chamber. The source chamber has a radius of 9 cm and a height of 12 cm, and it is made of aluminum, with a quartz plate on the top. Microwave power at 2.45 GHz (SGM-15A, DAIHEN) is supplied through the quartz at the top of the source chamber to generate plasma. The tuner (CMC-10, DAIHEN) matches the impedance of the ECR plasma automatically, which adjusts the reflected power to a zero value. The downstream chamber, made of aluminum and shaped as a rectangular parallelepiped, is composed of two parts. The upper one is 40 cm in width, 40 cm in depth, and 12 cm in height, and it is positioned coaxially to the source chamber. The lower one is 70 cm in width, 40 cm in depth, and 24 cm in height. The two external coils are at the upper and lower positions, respectively, each separated by 7 cm from the quartz plate. A circular plate of IG-430 isotropic nuclear grade graphite 45 mm in radius and 5 mm thick was prepared

for the deuterium ion irradiation. ECR plasma was generated with an operating deuterium gas pressure of 1 mTorr, microwave power range of 400 - 600 W, and coil current of 110 A. The ECR zone, whose magnetic field was 875 G, was ~207 mm from the target, as shown in Fig. 2.2, and its area was ~3.31 cm^2 owing to the conservation of the magnetic flux [23]. High energy electrons that are generated by resonance heating sustain a discharge at a low pressure gas. The plasma diffuses along the magnetic field lines into a downstream chamber toward a graphite target. A Langmuir probe was used to measure the plasma properties near the center of a graphite target [23], recording a plasma density range of 1 - 3.5 × 10^{11} cm^{-3} and an electron temperature range of 3.5 - 5.5 eV. In addition, the ion energy range of 17 - 100 eV was controlled by the target bias, which will be interpreted in detail in the following section. The ion fluxes were estimated according to the Bohm flux model to be within the range of 3.1 - 4.9 × 10^{17} $cm^{-2}s^{-1}$. This is similar to the ion flux of the planar, inductively coupled deuterium plasma [14], 3 × 10^{17} $cm^{-2}s^{-1}$, but lower than that of the divertor plasma simulator of PISCES-B: ~6 × 10^{18} $cm^{-2}s^{-1}$, with an electron density of 3 × 10^{12} cm^{-3} and an electron temperature of 6 eV [15]. The experimental conditions are prepared to simulate the far SOL plasma interaction with the graphite PFC in KSTAR, especially the effects of the ion irradiation energy on the morphological changes of the KSTAR divertor target [24]. In

addition to the ion irradiation energy, the dose of the ions was controlled by the ion irradiation time for the analysis of the effect of the total transferred energy on the graphite morphology, as Chapter 3 discusses in detail. The surface temperature of the graphite was measured using a pyrometer (MB35, Metis), as shown in Fig. 2.3. The measured surface temperatures were used to calculate the chemical sputtering yield. The effect of the recycled deuterium on the plasma properties with respect to the surface temperature was not particularly considered, because the maximum surface temperature was lower than 750 K, which is the first H_2 desorption peak of isotropic graphite [25]. This condition may ensure that the increment of the sputtering yield can be generated by the morphological changes of graphite. The partial pressures of neutral species were measured during the experiments using a residual gas analyzer (XT300, Extorr). In particular, the deuterated carbon species that were generated at a graphite target were measured according to the compensation of residual gas signals under the same experimental conditions as used for the stainless steel target. The sputtering yields of the graphite were determined according to the weight loss method [20, 26], by measuring the weight of the graphite before and after the plasma irradiation using an electronic scale with an accuracy of 10 μg.

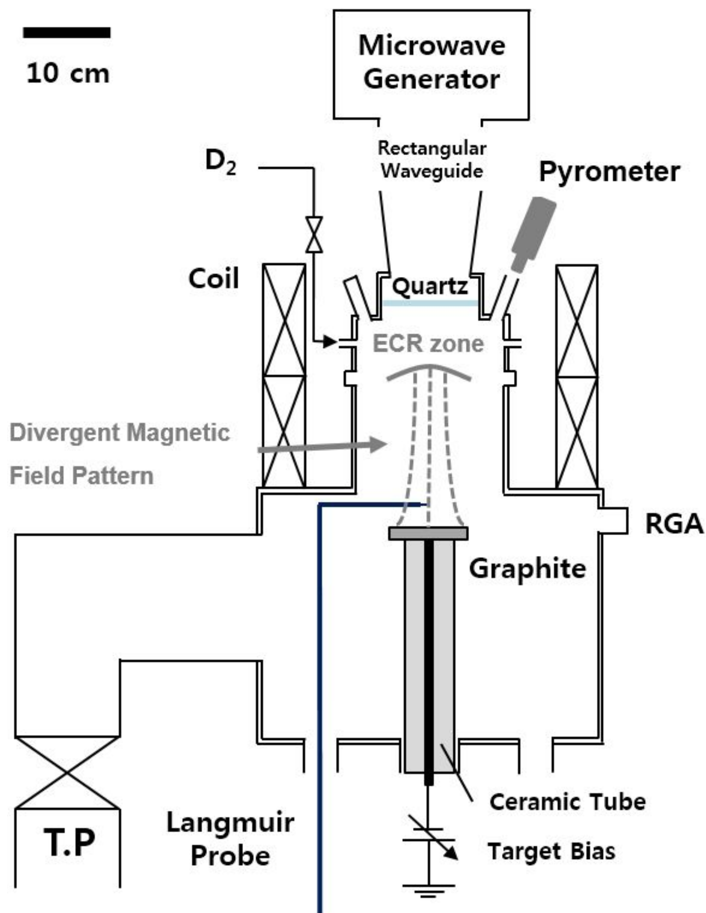

Figure 2.1. Schematic diagram of an ECR chamber for deuterium ion irradiation of graphite.

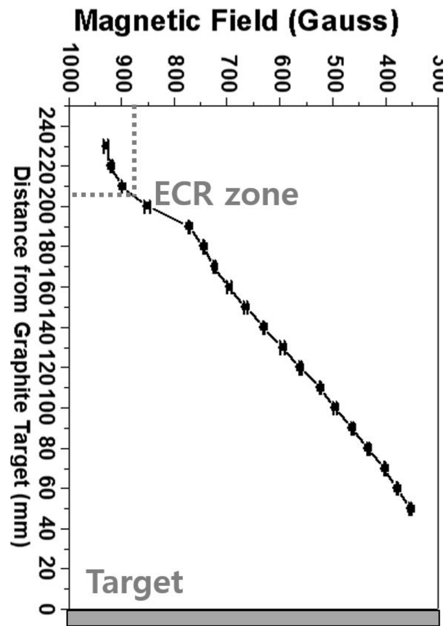

Figure 2.2. Magnetic field distribution with the distance from graphite target in an ECR chamber at a coil current of 110 A.

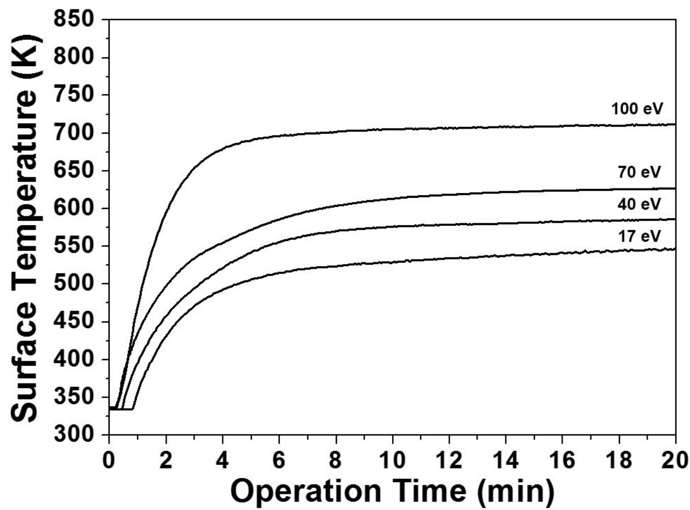

Figure 2.3. The variation of the surface temperature for an incident ion energy range of 17 – 100 eV in the ECR chamber.

The experimental setup using ECR plasma is employed to achieve the following characteristics. Firstly, the incident ion has a monotonic energy with a high flux. The ECR plasma is generated at a relatively low pressure by resonance heating, which brings the advantage of the collisionless sheath condition [23]. For the collisionless sheath where the ion gains energy [23], the deuterium ions maintain their energy and flux until they reach the target. This ensures the precise control of the incident ion energy by the sheath potential and the precise calculation of the sputtering yield of the graphite. Secondly, the main interaction area of the plasma is a graphite target. Because the plasma is usually generated in the stainless steel chamber, the stainless steel can be a main interaction area for the plasma. The strong axial magnetic field of the ECR plasma suppresses the radial diffusion of the plasma [23], resulting in a graphite target being the main interaction area. Thirdly, the ion incidence angle is normal to the surface of a graphite target. This ensures the incrementing of the carbon impurity formation by the morphological change of the graphite in comparison with a plane surface.

2.2. Determination of Ion Irradiation Conditions for DC Biased Target

A deuterium ion that passes through the sheath formed on the target gains energy equivalent to the sheath potential [23], and the energy of the irradiated ion can be varied according to the bias on the target. The energy of an ion is expressed as

$$E_i = e\left(V_p - V_t\right) = eV_s \tag{2.1}$$

Here, E_i is the energy of the ion, V_p is the plasma potential, V_t is the target bias potential, and V_s is the sheath potential. The measured plasma potential distribution is shown in Fig. 2.4(a). Operational conditions such as the deuterium pressure, coil current, and microwave power remain unchanged as the target bias potential is varied, which provides the independence of the bias effect from plasma properties such as the plasma potential, electron density, and electron temperature. Thus, the energy of the ions is independently controlled according to the target bias potential.

The deuterium ion dose can be varied according to the ion irradiation time, as follows:

$$D_i = \Gamma_i t = n_s \sqrt{\frac{kT_e}{M}} t \tag{2.2}$$

Here, D_i is the ion dose, Γ_i is the flux of the ion, t is the ion

irradiation time, n_e is the electron density, k is the Boltzmann constant, T_e is the electron temperature, and M is the ion mass. Because the collisionless sheath is assumed in the experimental setup as Chapter 2.1 discussed in detail, the Bohm sheath criterion is applied in the calculation of the ion flux [23]. In addition, the Bohm velocity is usually used when the ions are generated only within the source chamber and flow out of the source in ECR plasma [23]. The measured electron density and electron temperature distributions are shown in Fig. 2.4(b). The ion dose is varied by changing the ion irradiation time, rather than by modifying the bias potential or operating power, which indicates the capability to independently control the ion dose at constant plasma conditions.

Because the collisionless sheath was assumed, and the sheath potential range of 17 – 100 eV was larger than the electron temperature range of 4 – 5 eV, the sheath electric field was calculated using Child's Law [23]:

$$E_{sh} = \frac{4}{3}\frac{V_o}{d} = \frac{4}{3} \times \frac{V_o}{0.6\lambda_D (2V_0/T_e)^{3/4}} \tag{2.3}$$

Here, d is the sheath thickness, and λ_D is the Debye length. A sheath electric field up to 4.9×10^5 V/m was chosen to satisfy the fusion edge plasma condition because the sheath electric field near the limiter surface in TEXTOR is approximately 2×10^6 V/m [7].

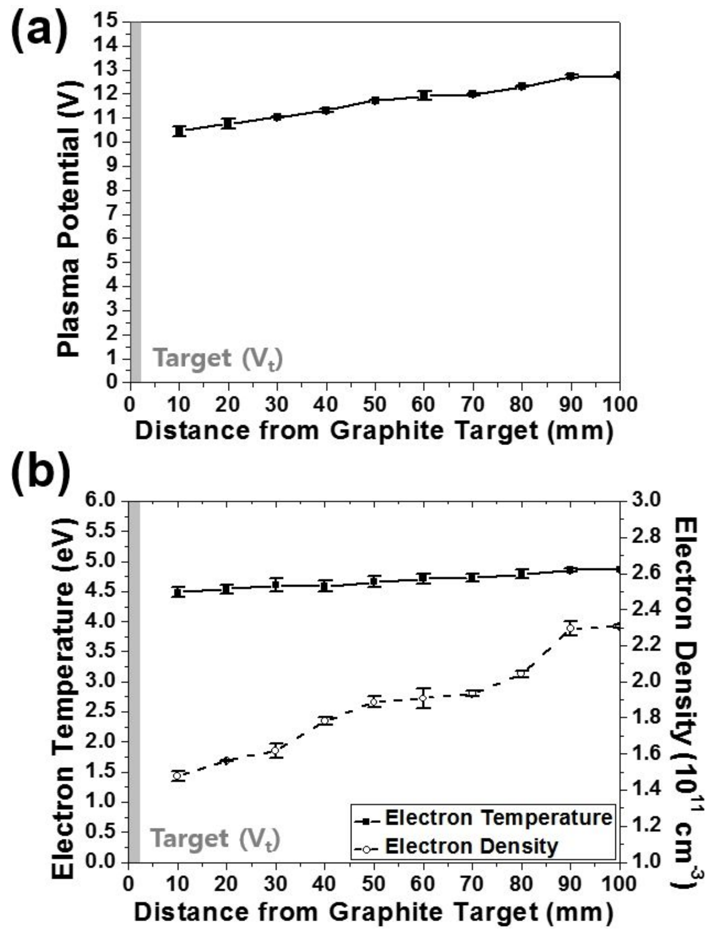

Figure 2.4. (a) Plasma potential, (b) electron temperature (filled squire with solid line) and electron density (empty circle with dotted line) in an ECR chamber at a deuterium pressure of 1 mTorr, a coil current of 110 A, microwave of 400 W.

2.3. Determination of Ion Irradiation Conditions for Pulse Biased Target

For a high sheath electric field with a low ion dose, a pulsed bias up to 1 kV was supplied to the target. As shown in Fig. 2.5, a sheath electric field range of 1.71 – 4.55 $\times$ 10^5 V/m was selected to satisfy the fusion edge plasma condition [7]. The sheath electric field was controlled by varying the target bias with the pulse system, and the stable plasma was sustained during the operation. The pulse system was operated for 100 ms (10 Hz), and the pulse length on the load was in the range of 130 – 200 μs, as shown in Fig. 2.6. The pulse bias comprised a rapid pulse rise, long plateau, and slow fall time; the plateau time was approximately 80% of the total pulse time. Here, the sheath electric field was estimated using the bias voltage on the pulse plateau time because the applied voltage was almost constant with a long pulse plateau time, compared with the ion plasma response time. The Child Langmuir sheath model was adopted to estimate a flux of ion and a dose of ion on a graphite target during the pulse plateau period [23]. Ions with high energies such as 300, 500, and 1000 eV, which correspond to high-energy ion incidence in the edge-localized mode (ELM), were irradiated during the operation. For example, ions with energies exceeding

500 eV have been detected during type-I ELMs in a tokamak [27]. Note that the energy of the incident ions, which corresponds to the sheath potential, is determined by using the potential difference between the plasma potential and the target bias [23]. It is assumed that the effects of the secondary electron emission due to the target surface are not serious, because high energy ions were only irradiated during the pulse period of 2 ms during 1 s of duty time. Operational conditions such as the deuterium pressure, coil current, and microwave power remain unchanged as the target bias potential is varied, which provides the independence of the bias effect from plasma properties such as the plasma potential, electron density, and electron temperature. Thus, the energy of the ions is independently controlled according to the target bias potential. The surface temperature of the graphite sample was saturated near 545 K after 1200 s, as shown in Fig. 2.3 for the zero-bias condition. Under these conditions, the incident ion energy was determined as 17 eV, which corresponds to the sheath potential. Because the high energy ions were only irradiated in 2 ms during 1 s of duty time, the surface temperature of the graphite did not increase remarkably and was maintained at 545 K during the irradiation. The effects of ion sputtering on the surface are probably not significant. The bulk plasma is not varied and the sheath electric field is independently controlled according to the target bias potential, resulting in the unconcern of the temperature effect on

the graphite and the chemical erosion.

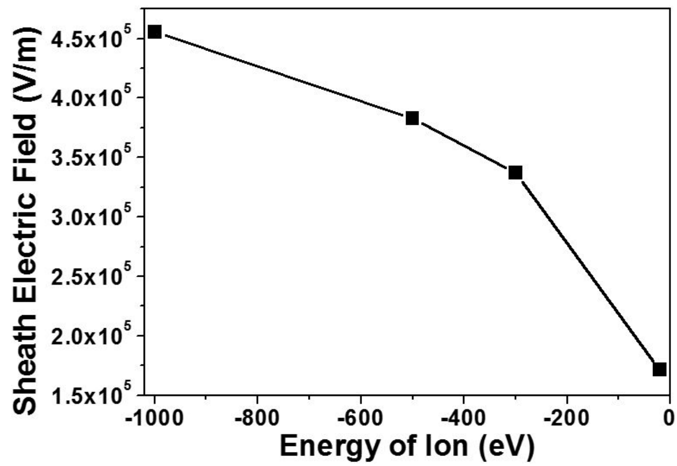

Figure 2.5. The variation of a sheath electric field with the target bias potential, as calculated with equation (2.3).

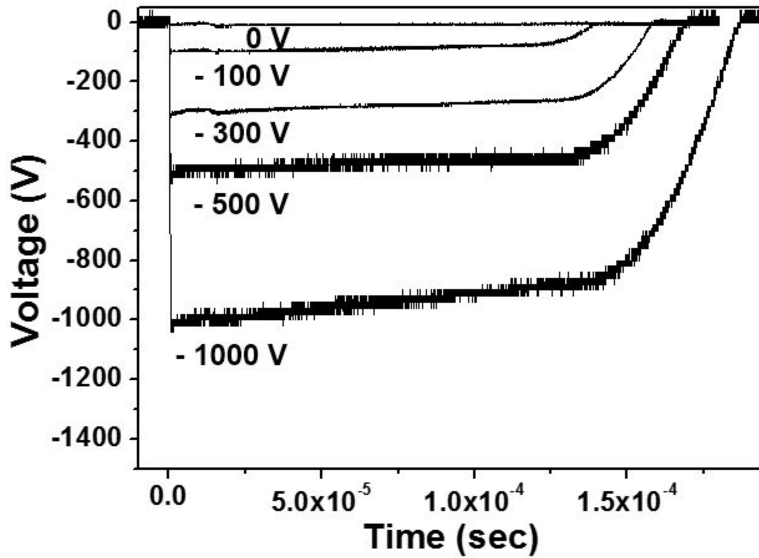

Figure 2.6. The variations of the target bias potential with pulse period on the target for various pulse bias voltages show the rapid pulse rise and slow fall time. The pulse system was operated for a duration of 100 ms (10 Hz) with a pulse length on load in the range 130 to 200 μs.

Chapter 3. Increment of Carbon Impurity Formation by Morphological Change of Graphite

3.1. Energy Dose for Morphological Change of Graphite Irradiated by Deuterium Plasma

As already discussed in Chapter 1.2, a carbon impurity is defined as C atoms and deuterated carbon (C_xD_y) molecules without the fuel gas of deuterium, and graphite morphology is variously changed by deuterium plasma irradiation. In particular, various parameters such as ion energy (E_i), ion flux (Γ_i), ion irradiation time (t) and temperature (T_{target}) determine the morphological change of graphite. Thus, a representative parameter, which considers the material deformation and plasma conditions, is required to analyze the morphological change of graphite. Except cracks and surface erosion by the binder material [13] and high surface temperature [14], respectively, the energy dose is established by consisting of the plasma physical properties. The energy dose is defined as

$$\boldsymbol{Energy\ Dose} = \boldsymbol{E_i} \times \boldsymbol{\Gamma_i} \times \boldsymbol{t} \tag{3.1}$$

The energy dose represents the total transferred energy on the graphite per unit area. The energy dose is deduced from the our previous study [28] about the averaged energy gain of C atom by considering energy dissipation depth [29]. The energy dose is employed to achieve the following characteristics. Firstly, the energy dose is used to develop the standard for analysis of the graphite deformation mechanism. Secondly, the morphological change of graphite with an operation condition is analyzed on the basis of the energy dose. Thirdly, the direction of the morphological change is estimated by extrapolation from its rate of change. For example, morphological changes of graphite are roughly similar in energy doses of 60.8 MJ/m^2 and 53.8 MJ/m^2 as shown in Figs. 3.1(a) and 3.1(b), respectively. Conical tip formation on the graphite surface is shown in both the Figs. 3.1(a) and 3.1(b). Because the energy dose does not consider the temperature effect on the morphological change of graphite, it can not be applied to analyze severe conditions, especially high surface temperature, such as ELM in fusion plasma. The energy dose is used to analyze the deuterium plasma - graphite surface interaction up to KSTAR SOL plasma steady-state condition.

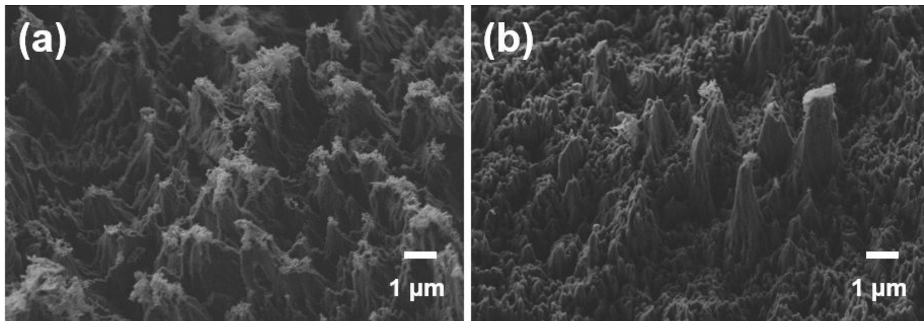

Figure. 3.1. SEM images of graphite samples after ion irradiation with (a) an ion energy of 40 eV and an ion dose of 9.5×10^{20} cm^{-2}, and (b) an ion energy of 70 eV and an ion dose of 4.8×10^{20} cm^{-2}. Energy doses are (a) 60.8 MJ/m^2 and (b) 53.8 MJ/m^2.

3.2. Morphological Change of Graphite by Deuterium Plasma Irradiation

3.2.1. Morphological Change of Graphite with Energy Dose

Morphological changes of graphite by the ion irradiation are shown in Figs. 3.2(a)-(c). Morphological changes of graphite by the ion irradiation and thermal load are shown in Figs. 3.2(d) and 3.2(e). It notes that the energy dose is calculated using Eq. (3.1). Nanoscale conical tip is generated on the graphite surface at the energy dose of 0.32 MJ/m^2 as shown in Fig. 3.2(a). Microscale conical tip is generated on the graphite surface at the energy dose of 6.8 MJ/m^2 as shown in Fig. 3.2(b). The formation mechanism of the conical tip will be interpreted in detail in the following section. Cone-shaped carbon bundle owing to the gathering of small conical tips is generated on the graphite surface at the energy dose of 152 MJ/m^2 as shown in Fig. 3.2(c) and this will be interpreted in detail in the following section. Conical tip with eroded surface is generated on the graphite surface at the energy dose of 5108 MJ/m^2 as shown in Fig. 3.2(d). In this condition, the thermal load of 15 MW/m^2 is irradiated ~5 min after an ion irradiation with an energy of 100 eV and a ion dose of 3.8×10^{21} cm^{-2}. Conical tip with eroded surface is also generated on the 2011 KSTAR divertor graphite

target at the energy dose of 9000 MJ/m^2 as shown in Fig. 3.2(e). In this condition, it is assumed that the ~1300 shots with an average irradiation time of 7 sec and an average heat flux of 1 MW/m^2 per each shot [30]. Figure 3.3 shows the morphological change of graphite with the energy dose, corresponding to the increment of conical tip size with the energy dose. Deuterium ion irradiation generates conical tips on the graphite as shown in Figs. 3.2(a, b, c), and conical tips and eroded surface are coexist as shown in Figs. 3.2(d) and 3.2(e). Consequently, the deuterium ion irradiation generates the conical morphology of graphite and the thermal load generates the eroded surface of graphite.

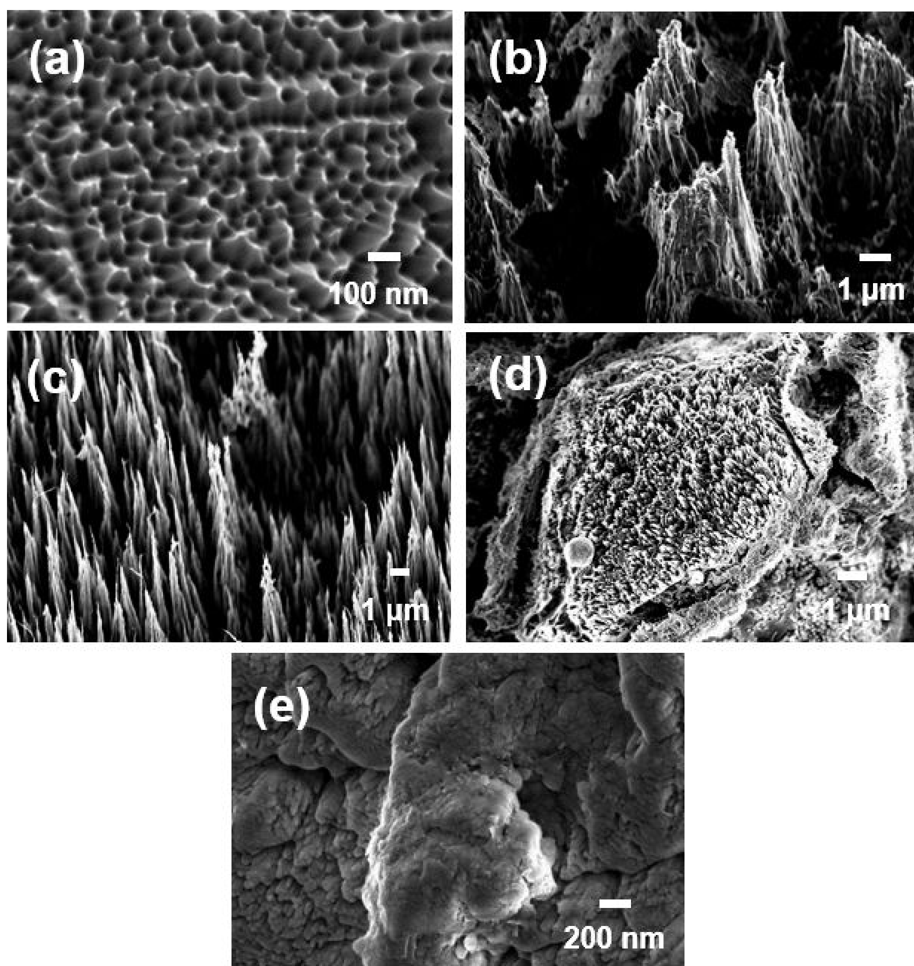

Figure. 3.2. (a) Nanoscale conical tip formation at the energy dose of 0.32 MJ/m^2. (b) Conical tip formation at the energy dose of 76.8 MJ/m^2. (c) Cone-shaped carbon bundle formation at the energy dose of 152 MJ/m^2. (d) Conical tip with eroded surface at the energy dose of 5108 MJ/m^2. (e) Conical tip with eroded surface at the energy dose of 9000 MJ/m^2.

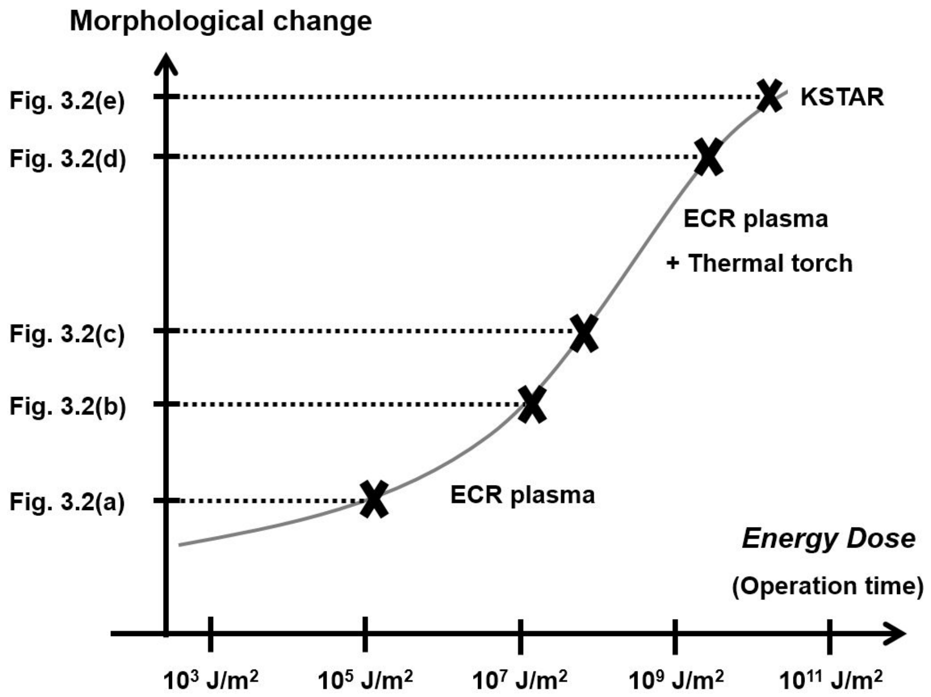

Figure. 3.3. Morphological change of graphite with the energy dose.

3.2.2. Formation Mechanism of Conical Tips on Graphite

Morphologically changing progress of graphite by the deuterium ion irradiation was analyzed using energy dose, and formation of conical tips on the graphite surface was a representative morphology. As discussed in Chapter 1.2.2, the incrementing of the ion incidence angle caused by the morphological change of graphite can increase the sputtering yield. Thus, the graphite morphology by the deuterium ion irradiation has to be defined to establish the sputtering yield model and to estimate the sputtering yield at the deuterium ion irradiation condition. Analysis of the formation mechanism of conical tips on the graphite can be used to define the graphite morphology, i.e., height, diameter, and aspect ratio of conical tip, at the deuterium ion irradiation condition.

Figure 3.4 shows SEM images of graphite before and after ion irradiation at a dose of 5×10^{16} cm^{-2}, and Fig. 3.5 shows the Raman spectra of graphite under the same conditions as in Fig. 3.4. The material characteristics, including the in-plane crystallite size (La value), the out-of-plane stacking order, and the disorder or defects of the graphite samples, can be determined from the peaks of the so-called G and D bands at 1582 and 1350 cm^{-1} respectively. The presence of disorder in a sp^2-hybridized carbon system leads to an increase in the intensity of the D band. Figure 3.4(a) shows a SEM micrograph of pristine graphite,

which has a typical polycrystalline morphology [31, 32] and I_D/I_G of 0.255. After deuterium ion irradiation with a sheath electric field of 3.37 × 10^5 V/m and an ion dose of 5 × 10^{16} cm^{-2}, the surface of the graphite sample becomes roughened and then nanoscale dot-like structures are generated, as shown in Fig. 3.4(b) and clearly evident from the comparison with the pristine graphite. I_D/I_G of the ion irradiated graphite with a sheath electric field of 3.37 × 10^5 V/m is increased up to 0.956 in comparison with the pristine graphite. The increase in I_D/I_G that results from ion irradiation indicates that there is a decrease in the in-plane crystallite size [33] and an increase in the amount of disorder and defects. Here, the disorder and defects are due to sp^3 character and hydrogenated bonding. The number of dot-like structures increases and they become more uniformly distributed when a sheath electric field is increased to 3.83 × 10^5 V/m, as shown in Fig. 3.4(c). I_D/I_G of the ion irradiated graphite with a sheath electric field of 3.83 × 10^5 V/m is similar to that for the graphite with a sheath electric field of 3.37 × 10^5 V/m. The Raman results and the SEM images reveal that the nanoscale dot-like structure formed by the ion irradiation consists of mixed sp^2-sp^3 character and hydrogenated bonding [34, 35]. Some portion of the sp^3 character originates from nanodiamond produced by high energy ion irradiation, as confirmed in previous reports [36, 37]. When a sheath electric field is increased further to 4.55 × 10^5 V/m, the size of the dot-like structures increases to

approximately 35 nm to produce the cone-shaped structures shown in Fig. 3.4(d). This structure probably grows from the carbon dot-like structures as a result of the plasma - surface interaction on the graphite. From the observation of the drastic increase in the I_D/I_G value of the sample treated with a sheath electric field of 4.55 × 10^5 V/m, we conclude that the conical tip is composed of more disordered and defected-carbon bonding than the nanoscale dot-like structure.

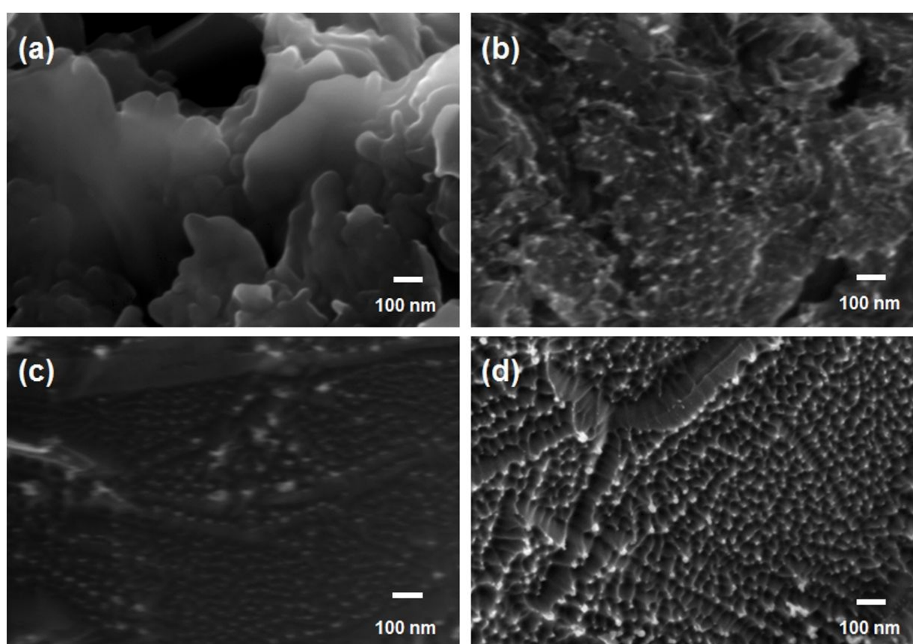

Figure. 3.4. SEM images of graphite (a) before and (b)-(d) after ion irradiation at a dose of 5 × 10^{16} cm^{-2}. Sheath electric fields are (b) 3.37 × 10^5 V/m, (c) 3.83 × 10^5 V/m, and (d) 4.55 × 10^5 V/m.

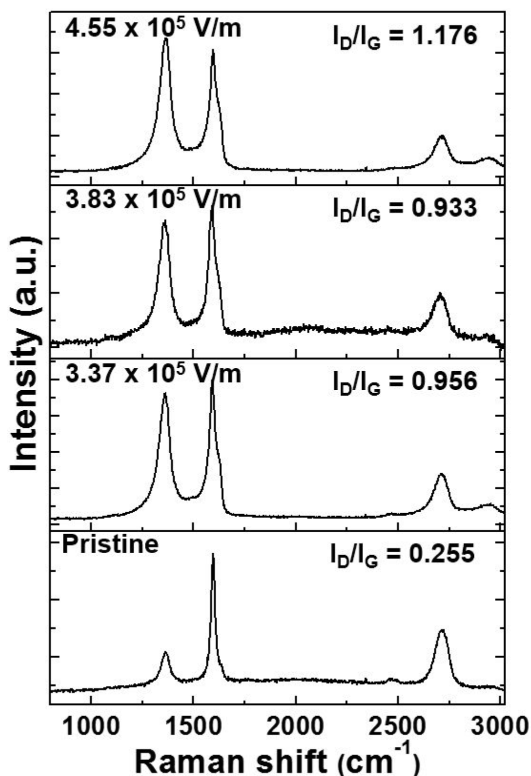

Figure. 3.5. Raman spectra of pristine (before irradiation) and ion irradiated graphite; an ion dose was 5×10^{16} cm^{-2}.

The conical tip was analyzed to have the composition of more disordered and defected-carbon bonding than the nanoscale dot-like structure. When a dose of ions is increased with ion irradiation time, the size of conical tip can be increased as expected in the Chapter 3.2.1 due to the increased energy dose i.e. total transferred energy on the graphite. Figure 3.6 shows SEM images of the graphite samples after ion irradiation with various ion doses at a sheath electric field of 4.55×10^5 V/m. A

few nanometer-sized conical tips are present on the surface of the graphite sample after irradiation with an ion dose of 1 × 10^{16} cm^{-2}, as shown in Fig. 3.6(a). In Figs. 3.6(b)-(e), it is clear that the size of the tips increases with increases in the dose of ions, as summarized in Fig. 3.6(f). Figure 3.7 shows the Raman spectra for the samples in Figs. 3.6(a)-(e). As indicated in Fig. 3.7, I_D/I_G does not vary significantly with an ion dose and it implies that the conical tips are once formed and not grown. This result also implies that the conical tips are composed of more disordered and defected-carbon bonding. In addition, it shows that the larger tips are formed through a tip-tip bonding process, not through top growth or bottom growth. This growth model will be discussed in the following section together.

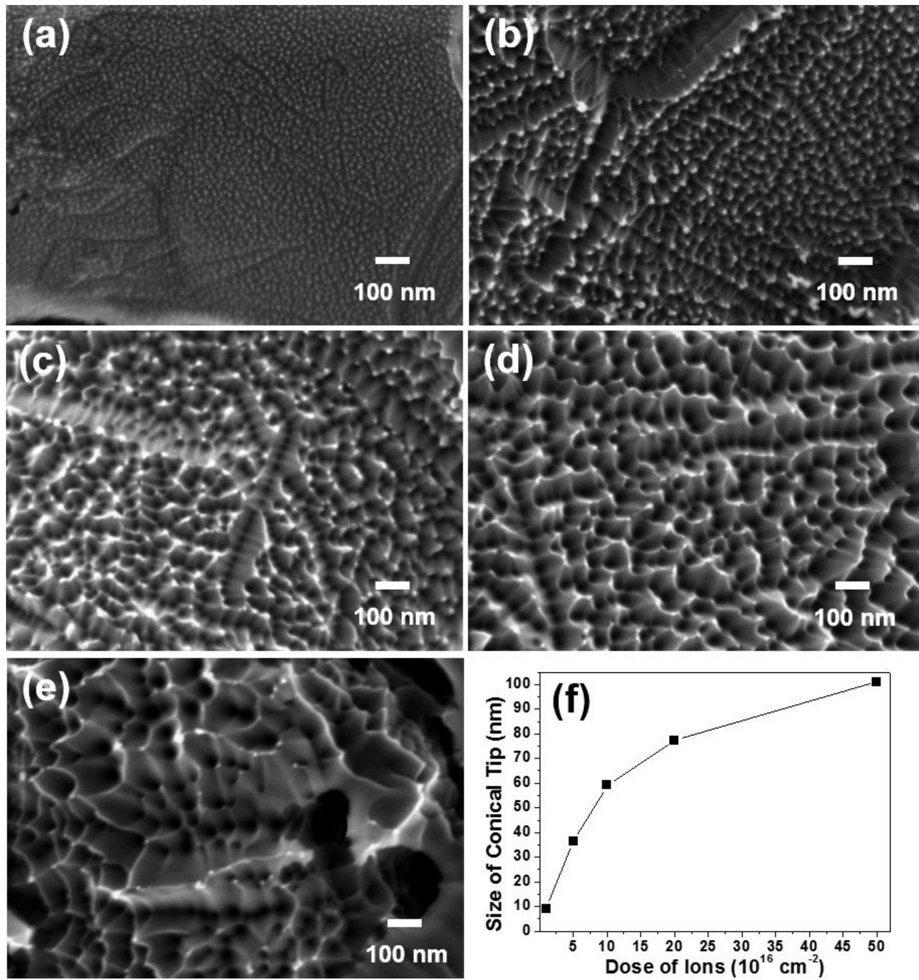

Figure. 3.6. SEM images of graphite samples after ion irradiation with a sheath electric field of 4.55 × 10^5 V/m and various ion doses: (a) 1 × 10^{16} cm^{-2}, (b) 5 × 10^{16} cm^{-2}, (c) 1 × 10^{17} cm^{-2}, (d) 2 × 10^{17} cm^{-2}, and (e) 5 × 10^{17} cm^{-2}. (f) The variation in the size of the conical tips with a dose of ions.

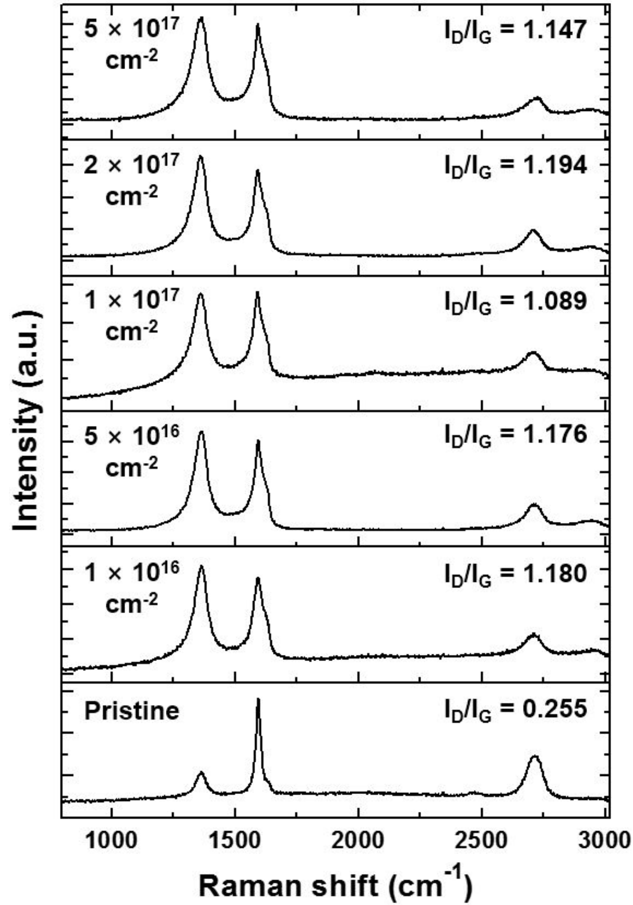

Figure. 3.7. Raman spectra of pristine graphite (before irradiation) and ion irradiated graphite irradiated with a sheath electric field of 4.55×10^5 V/m and various ion doses: 1×10^{16} cm^{-2}, 5×10^{16} cm^{-2}, 1×10^{17} cm^{-2}, 2×10^{17} cm^{-2}, and 5×10^{17} cm^{-2}.

3.2.3. Formation Mechanism of Cone-shaped Carbon Bundle on Graphite

Conical tip formation on the graphite surface by the deuterium ion irradiation was discussed in Chapter 3.2.2. The early stage of the conical tip formation was analyzed at a relatively low ion dose range of 1×10^{16} cm^{-2} - 5×10^{17} cm^{-2} by using the pulse biased target, as Chapter 2.3 discussed in detail. Because an ion dose up to 10^{24} [1-4] and a sheath electric field up to 2×10^{6} V/m [7] are expected in the fusion devices, the morphological change of graphite at a high ion dose and a high sheath electric field will be analyzed in this chapter. This will contribute to establish the sputtering yield model and to estimate the sputtering yield at the deuterium ion irradiation condition.

Figure 3.8 shows SEM images of the thirty degree tilted graphite samples after ion irradiation at constant ion flux of 1.8×10^{17} $cm^{-2}s^{-1}$. At an ion dose of 4.8×10^{20} cm^{-2} with an ion energy of 40 eV and a sheath electric field of 3×10^{5} V/m, the surface of graphite sample becomes roughened as shown in Fig. 3.8(a). When an ion dose is increased up to 9.5×10^{20} cm^{-2}, a few hundreds of nm sized conical tips are generated, as shown in Fig. 3.8(b). Similar morphology was observed in the deuterium plasma ion irradiation at an ion energy of 30 eV by Balden et al [14] and 40 eV by Balwen et al [15]. They explained that the conical tip was formed by smearing out the directional structure

by the thermal D from the plasma exposure [14]. When an ion energy is increased further to 100 eV with a sheath electric field of 3.8×10^5 V/m, the sharper tips are generated as shown in Fig. 3.8(c). The size of tip is increased with a dose of ion as shown in Fig. 3.8(d). This implies that the directional impact of the energetic ions enhances the depth of the sputter etch, resulting in the formation of the sharper tip than that for the irradiated ion energy of 40 eV.

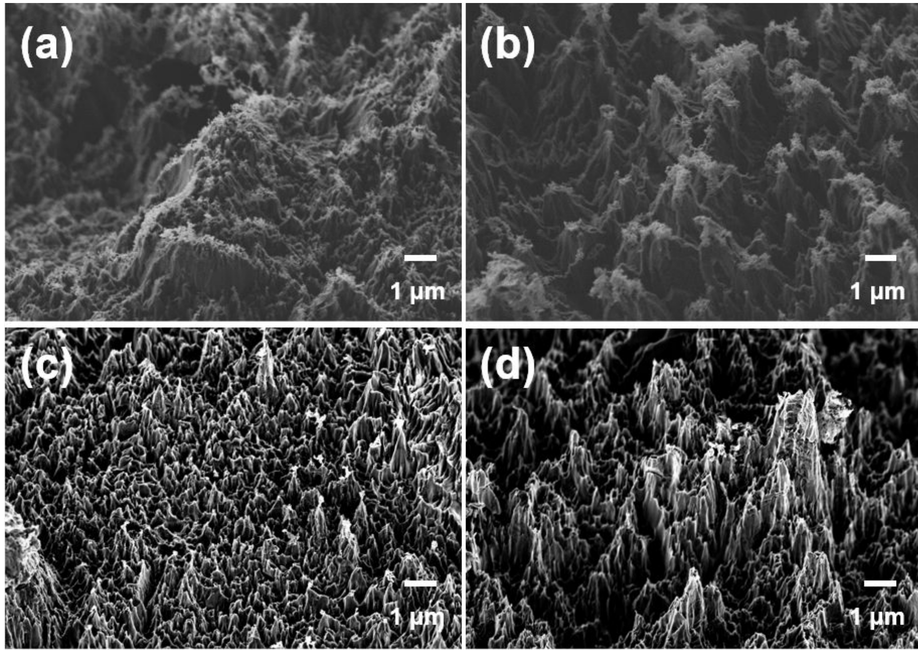

Figure. 3.8. Thirty degrees tilted SEM images of graphite after ion irradiation at constant ion flux of 1.8×10^{17} $cm^{-2}s^{-1}$. The ion irradiation conditions are (a) an ion energy of 40 eV, a sheath electric field of 3×10^5 V/m, and an ion dose of 4.8×10^{20} cm^{-2}, (b) an ion energy of 40 eV, a sheath electric field of 3×10^5 V/m, and an ion dose of 9.5×10^{20} cm^{-2}, (c) an ion energy of 100 eV, a sheath electric field of 3.8×10^5 V/m, and an ion dose of 4.8×10^{20} cm^{-2}, and (d) an ion energy of 100 eV, a sheath electric field of 3.8×10^5 V/m, and an ion dose of 9.5×10^{20} cm^{-2}.

Figure 3.9 shows SEM images of the top and thirty degree tilted graphite samples after ion irradiation with a constant ion energy of 100 eV and a sheath electric field of 4.9×10^5 V/m. As shown in Figs. 3.9(a) and 3.9(b), the conical tips are more sharper than that for the ion irradiated graphite at an ion energy of 100 eV and a sheath electric field of 3.8×10^5 V/m. It implies that a sheath electric field affects the formation of conical tips on the graphite to align the direction of a sheath electric field, which is normal direction of the graphite surface. It is observed that the size of the conical tips increases with increases in the dose of ions as shown in Figs. 3.9(c)-(f). In particular, the cone-shaped carbon bundle formation is generated by the gathering of the small conical tips. A sheath electric field and a dose of ions are important factor for the cone-shaped carbon bundle formation on the graphite surface, which was expected in our previous study of the formation mechanism of cone-shaped CNT bundles [38].

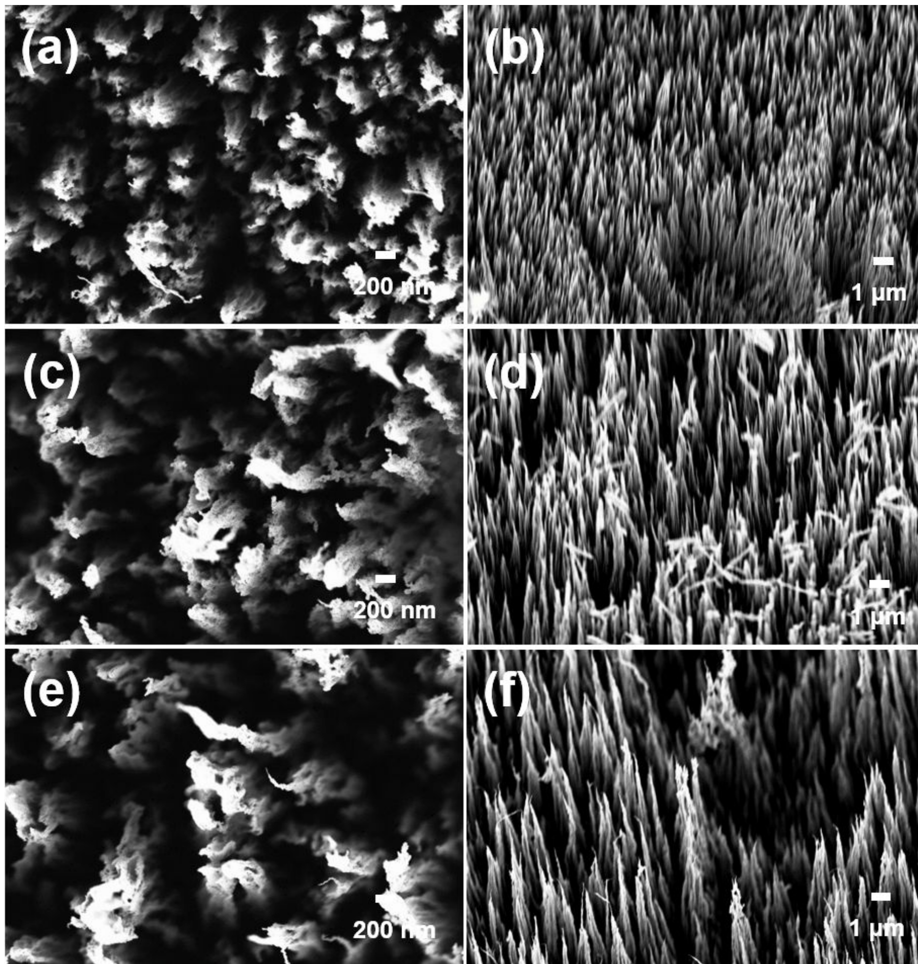

Figure. 3.9. Top (a, c, e) and thirty degrees tilted SEM images (b, d, f) of graphite after ion irradiation at constant ion energy of 100 eV, an ion flux of 2.8×10^{17} $cm^{-2}s^{-1}$, and a sheath electric field of 4.9×10^{5} V/m. Doses of ions are (a), (b) 9.5×10^{20} cm^{-2}, (c), (d) 1.9×10^{21} cm^{-2}, and (e), (f) 3.8×10^{21} cm^{-2}.

Figure 3.10 shows top-view SEM images of the graphite samples after an ion irradiation with various sheath electric fields at constant ion energy of 100 eV. Crack is generated after irradiation at a sheath electric field of 1.4×10^5 V/m with an ion dose of 2.3×10^{20} cm^{-2} as shown in Fig. 3.10(a), which is also shown in our previous study [13]. After an ion irradiation at a sheath electric field of 3.0×10^5 V/m with an ion dose of 9.5×10^{20} cm^{-2}, a few hundreds of nm sized conical tips are generated as shown in Fig. 3.10(b). The conical tips on the graphite surface is also generated at a sheath electric field of 4.9×10^5 V/m with an ion dose of 9.5×10^{20} cm^{-2} as shown in Fig. 3.10(c). In particular, the formation of the cone-shaped carbon bundle owing to the gathering of small conical tips, which corresponds to the tip-tip bonding process. Note that this shape can be obtained through neither the top growth nor the bottom growth. Thus, the cone-shaped carbon bundle formation is generated by the gathering of the conical tips instead of the continuous growth of the single tip as the growth of CNTs from the metal catalyst in chemical vapor deposition [39]. Because an ion energy of 100 eV is the same for Figs. 3.10(a)-(c), this result also implies that a sheath electric field is an important factor for the cone-shaped carbon bundle formation on the graphite surface as expected in the our previous study [38].

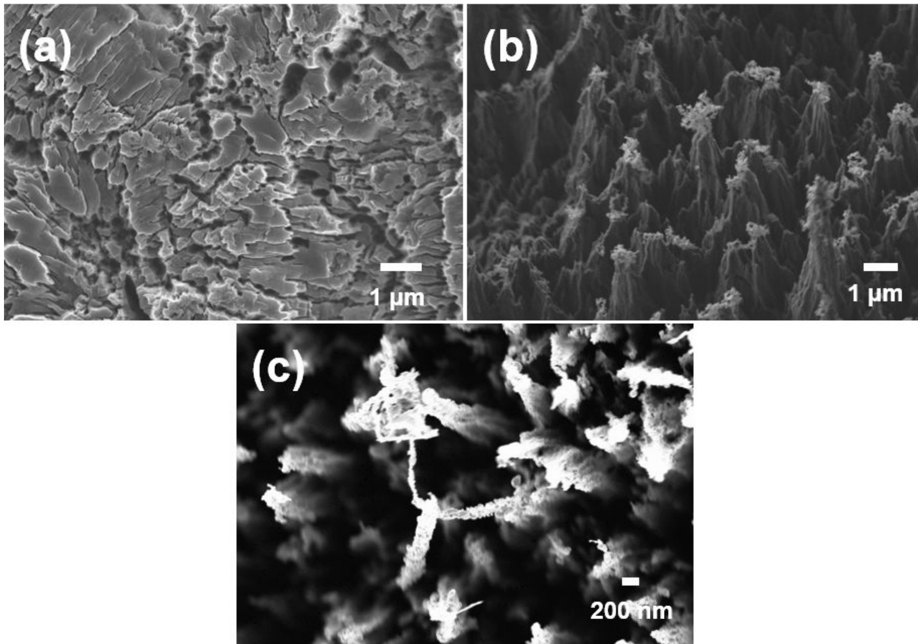

Figure. 3.10. Top-view SEM images of graphite after ion irradiation at constant ion energy of 100 eV. The sheath electric fields are (a) 1.4×10^5 V/m at an ion dose of 2.3×10^{20} cm^{-2}, (b) 3.0×10^5 V/m at an ion dose of 9.5×10^{20} cm^{-2}, and (c) 4.9×10^5 V/m at an ion dose of 9.5×10^{20} cm^{-2}.

We developed the formation mechanism of cone-shaped carbon bundles as shown in Fig. 3.11, which is similar to the formation of cone-shaped CNT bundles [38]. Figure 3.11(a) shows that an ion irradiation results in the initial stage of the formation of nanoscale conical tips on the top surface of the graphite sample. This can be caused by the formation of nanoscale dot-like structures which were partially composed of diamond-like carbon

[36], or the deposition of metal atoms from inner wall of the chamber [40, 41]. Diamond-like carbon can be generated at the top surface of the graphite, which was irradiated by high energy ion [36]. Diamond-like carbon has a much higher displacement threshold energy than graphitic carbon [42] such as metal atom. So the nanoscale dot-like structures which contain a small amount of diamond-like carbon are considered to have a slightly higher displacement threshold energy than graphitic atoms. The nanoscale dot-like structures and metal atoms act as a precursor due to their smaller sputtering yield and they grow to form conical tips with increases in the ion dose, as represented in Fig. 3.11(b). When the ion dose is increased further, conical tips with greater height are generated because the sputtering effect on the shoulder of the conical tip is larger than the welded apexes of the conical tip [38]. If a conical tip is considered as a point dipole, as suggested in our previous study of CNTs [38], the apexes of the conical tips are gathered by attractive dipole forces and welded by the continuous irradiation of ions. The attractive dipole force increases with a sheath electric field, so the cone-shaped carbon bundle formation is achieved with the increase of a sheath electric field. In addition, the polarizability of the conical tip increases with its size, which results in the increases in the size of the cone-shape carbon bundles with a dose of ions.

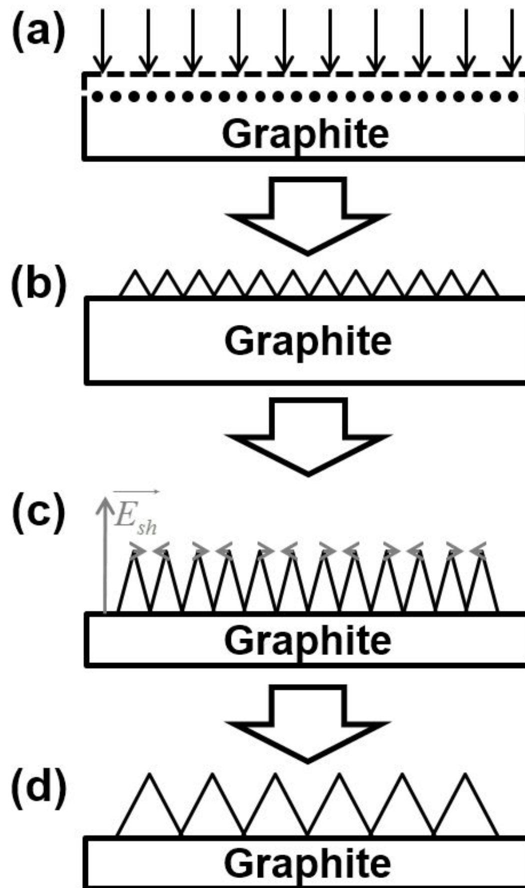

Figure. 3.11. Schematic diagram of the cone-shaped carbon bundle formation on the graphite: (a) formation of nanoscale dot-like structures by ion incidence or deposition of impurity atom from sample holder/inner wall of chamber act as a precursor; (b) initial conical tip formation is generated due to difference of sputtering yields; (c) conical tips with greater height are generated by increases in an ion dose; and (d) the cone-shaped carbon bundle formation through the collection and welding of adjacent conical tips due to attractive dipole forces.

A model based on the scenario described in Fig. 3.11 was developed for the case of the deuterium ion irradiations. Many C-D bonds at the graphite surface or the tiny size of the conical tip enhance the polarizability of the graphite, resulting in the enhancement of the induced dipole moment along the axis of the conical tip. Thus the induced dipole moment along the axis of the conical tip is increased with the number of C-D dipoles at the graphite surface, i.e., dose of deuterium ions. Note that this model does not consider the permanent C-D dipole and it rather considers the induced dipole moment along the axis of the conical tip. In addition, this model can be adapted in both the CNTs [38] and conical tips on the graphite surface because the induced dipole for each CNTs or conical tips is considered as a point dipole. The interaction force of the conical tip under a sheath electric field is described in Fig. 3.12. As shown in Fig. 3.12, the induced dipole moment along the axis of the conical tip is $\vec{p} = \alpha \vec{E}_{sh}$, here a is the polarizability and E_{sh} is an applied sheath electric field. The dipole interaction energy U between the conical tip 1 and the conical tip 2 is as follows [38]:

$$U = -\alpha_1 E_{sh}^2 (1 + \alpha_2 \frac{3\cos^2\theta - 1}{4\pi\varepsilon_0 r^3}) \qquad (3.2)$$

Here, a_1 is the polarizability of the conical tip 1, a_2 is the polarizability of the conical tip 2, Θ is the angle between the axis of the conical tip 2 and a sheath electric field, and r is the distance between the conical tip 1 and conical tip 2. From Eq.

(3.2), the dipole force between the conical tip 1 and the conical tip 2 is

$$\vec{F}_{dipole} = \frac{3\alpha_1\alpha_2 E_{sh}^2}{4\pi\varepsilon_0 r^4}(1-3\cos^2\theta)\hat{r} \tag{3.3}$$

Consider the induced dipole moment along the axis of the conical tip 2 as

$$p = \alpha_2 E_{sh}\cos\theta \tag{3.4}$$

The corresponded torque, τ, on the conical tip 2 under the sheath electric field is

$$\tau = \left|\vec{p}\times\overrightarrow{E_{sh}}\right| = \alpha_2 E_{sh}^2 \sin\theta\cos\theta \tag{3.5}$$

Then the aligning force, F_{align}, of the conical tip 2 can be described as

$$F_{align} = \tau / L = \alpha_2 E_{sh}^2 \sin\theta\cos\theta / L \tag{3.6}$$

Here, L is the height of the conical tip. From Eqs. (3.5) and (3.6), the net force on the conical tip can be obtained as

$$\vec{F} = \alpha_2 E_{sh}^2\left[\left\{\frac{\sin\theta\cos^2\theta}{L} + \frac{3\alpha_1}{4\pi\varepsilon_0 r^4}(1-3\cos^2\theta)\right\}\hat{r} + \frac{\sin^2\theta\cos\theta}{L}\hat{z}\right] \tag{3.7}$$

Here the first and second terms mean the attractive force F_{dipole} and the repulsive aligning force F_{align} in the radial direction, respectively, which should be balanced to form the bundle. The force in the normal direction (the third term in RHS of Eq. 3.7) is the force balanced with the surface adhesion of graphite.

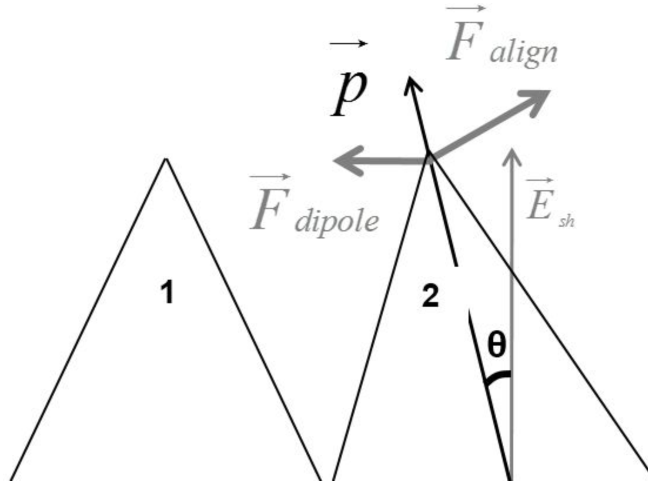

Figure. 3.12. Schematic of the interaction between the conical tip 1 and the adjacent conical tip 2. E_{sh} is a sheath electric field, $\vec{p}$ is the induced dipole moment along the axis of the conical tip 2, F_{align} is the aligning force, F_{dipole} is the dipole force, Θ is the angle between the axis of the conical tip 2 and a sheath electric field.

The applied force on the conical tip is proportional to a and E_{sh}^2, as derived in Eq. (3.6). For the sheath electric field up to 3.8×10^5 V/m, the cone-shaped carbon bundle formation by gathering of the small conical tips is not generated due to a low sheath electric field. For a sheath electric field of 4.9×10^5 V/m, however, the applied force on the conical tip is enough to bend the conical tips due to the attractive dipole force, resulting in the cone-shaped carbon bundle formation by gathering of the small conical tips as shown in Fig. 3.10(c). The polarizability of

cone-shaped carbon bundles, which correspond to Fig. 3.9, can be calculated from their diameters and heights by using Eq. (3.7),

$$\alpha = \frac{4\pi\varepsilon_0}{10^{18}} \frac{D^5}{12[H^2+(D/2)^2]} \times \frac{1-D^2/4[H^2+(D/2)^2]}{1-3D^2/8[H^2+(D/2)^2]} \quad (3.8)$$

Here, D and H are the diameter and height of the conical tip respectively. The units of D and H are μm and those of a are Cm^2V^{-1}. By using Eq. (3.8), the polarizability of a cone-shaped carbon bundle can be estimated from its diameter and height, which can be obtained with experimental measurements.

The units of the polarizability were converted to $Å^3$ since a $(Å^3)=(10^{30}/4\pi\varepsilon_0)\times a(Cm^2V^{-1})$. The polarizabilities of cone-shaped carbon bundles are in the range of 2.1×10^8 - 9×10^9 $Å^3$ for a sheath electric field of 4.9×10^5 V/m. The increases in the polarizability with the ion dose result in increases in the size of cone-shaped carbon bundles. The applied force on cone-shaped carbon bundles on graphite can be compared with the cone-shaped CNT bundles which are in the range 6.3×10^{10} - 2.5×10^{13} $Å^3$ for a sheath electric field of 6.1×10^3 V/m [38]. The applied force on conical tips is proportional to the polarizability, a, and a sheath electric field, E_{sh}^2, so the cone-shaped carbon bundle formation on the graphite is generated at larger sheath electric field than that for the CNTs, which have large polarizabilities because of their intrinsic tube structures and vertical orientations [38].

These results indicate that the formation of conical tips on the

graphite requires a sheath electric field of 3×10^5 V/m and the cone-shaped carbon bundle formation by gathering of the small conical tips requires a sheath electric field of 4.9×10^5 V/m. The edge plasma of ERO-TEXTOR was estimated to have a sheath electric field of 2×10^6 V/m [7], so the conical tips and the cone-shaped carbon bundles could form on the carbon-based walled fusion device. This observation would be related to the enhancement of the sputtering yield of graphite in fusion devices because the cone-shaped morphology may increase the local angle of ion incidence [20].

3.3. Increment of Sputtering Yield by Morphological Change of Graphite

3.3.1. Sputtering Yield Model with Consideration of Graphite Morphology

Because the morphology of graphite surface is not constant during ion irradiation as discussed in Chapter 3.2, it is required to deduce a representative morphology for the calculation of sputtering yield. Conical tip formation on the graphite surface by deuterium ion irradiation is chosen as a representative morphology in this study. For a constant energy of ion, i.e., constant sheath electric field, the diameter and height of the conical tip are increased with a dose of ions while maintaining almost constant aspect ratio as shown in Fig. 3.13. According to the results, it is assumed that the conical tip on the graphite surface keeps its aspect ratio during the morphological change of graphite with operation time. For a constant dose of ions, the diameter and height of the conical tip are increased with an energy of ion while its aspect ratio is increased as shown in Fig. 3.14. According to the results, it is assumed that aspect ratio of the conical tip, which determines the local angle of ion incidence, can be controlled by an energy of ion. In other words, graphite morphologies including the local angle of ion incidence are

controlled by the deuterium ion irradiation conditions.

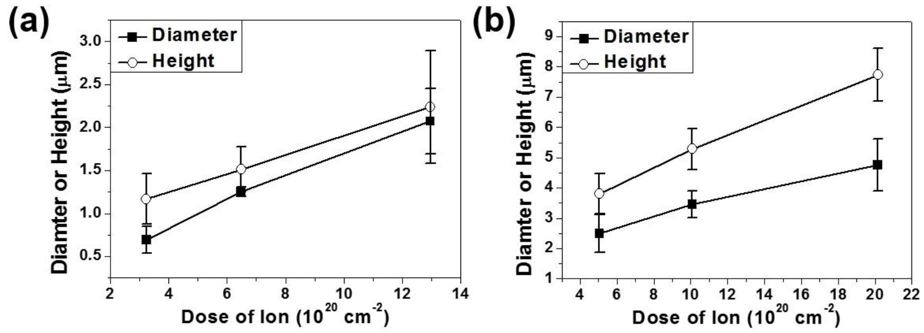

Figure. 3.13. Diameters (filled square) and heights (empty circle) of the conical tip on the graphite after ion irradiation at constant ion energy of 100 eV. Ion fluxes are (a) 1.8 × 10^{17} $cm^{-2}s^{-1}$ and (b) 2.8 × 10^{17} $cm^{-2}s^{-1}$.

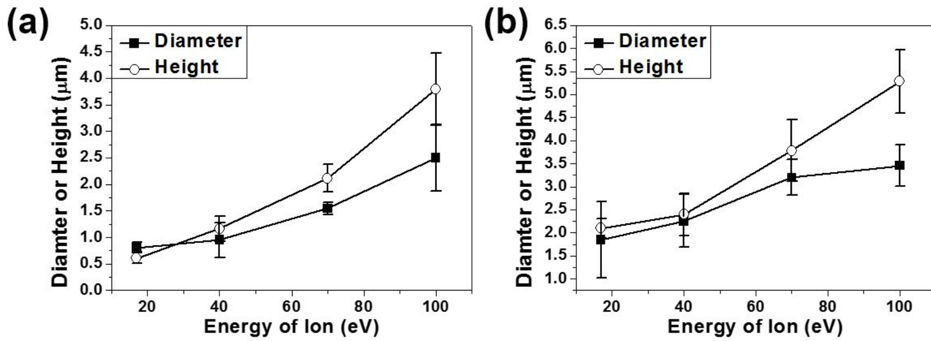

Figure. 3.14. Diameters (filled square) and heights (empty circle) of the conical tip on the graphite after ion irradiation at constant ion flux of 2.8 × 10^{17} $cm^{-2}s^{-1}$. Ion doses are (a) 4.8 × 10^{20} cm^{-2} and (b) 9.5 × 10^{20} cm^{-2}.

Sputtering yield model for the conical tip on the graphite surface is developed as depicted in Fig. 3.15. Because the magnetic field effect on the angle of ion incidence is removed by using the perpendicular magnetic field on the graphite, the local angle of ion incidence is determined by the graphite morphology. Local angle of ion incidence, σ, is determined from cone angle, ϕ, of graphite morphology with relation of $\sigma = 90 - \phi$. Backscattered ions in a neutral form leave the surface at an ion incidence point cosine distributed [20]. In the present model, it is assumed that the backscattered ions are irradiated on the neighboring cone with local angle of $|\pi - 3\sigma|$ for simplicity. Number of collisions by backscattered ions is determined by the local angle of incident ion. The contribution of the second and the other collisions by re-backscattered ion is very low due to its low energy in comparison with the first collision by backscattered ion. Thus, a single collision by backscattered ion in addition to the collision by incident ion is considered in the present model.

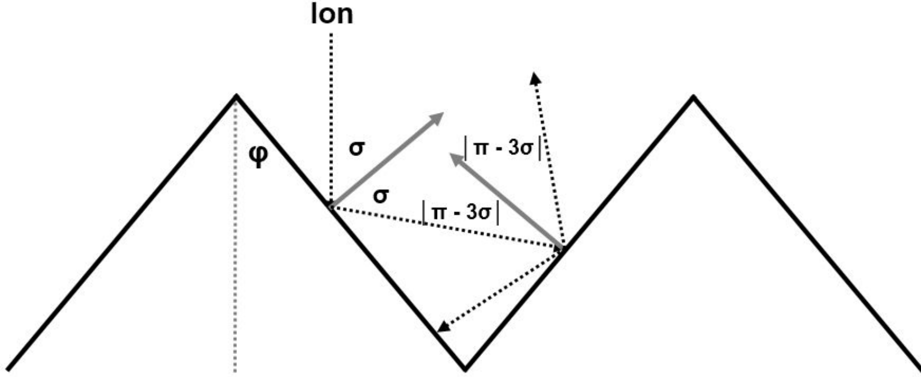

Figure. 3.15. Schematic illustration of the trajectory of ion incidence on the conical shaped graphite morphology. Ion is irradiated with local angle of σ due to cone angle of ϕ. Backscattered ion with form of neutral is irradiated on the neighboring cone with local angle of $|\pi - 3\sigma|$.

Physical and chemical sputtering yields for normal ion incidence on graphite are calculated from the Roth's formula [8]. Angular dependence on physical sputtering yield is calculated from Wei's formula [18] as

$$Y_{phys}^{1st}(E_i^{1st},\sigma) = Y_{phys}^{Roth}(E_i^{1st},\sigma=0)\times\cos\sigma\exp\left(\frac{a^2\sin^2\sigma}{2\alpha^2}\right) \tag{3.9}$$

Here, Y_{phys}^{1st} is physical sputtering yield by incidence of initial ion, E_i^{1st} is an energy of initial ion, Y_{phys}^{Roth} is physical sputtering yield of Roth model by incidence of initial ion, a is the projected energy range and a is the energy range straggling along the longitudinal direction. Energy ranges (a and a) are calculated by

TRIM [29] as shown in Fig. 3.16.

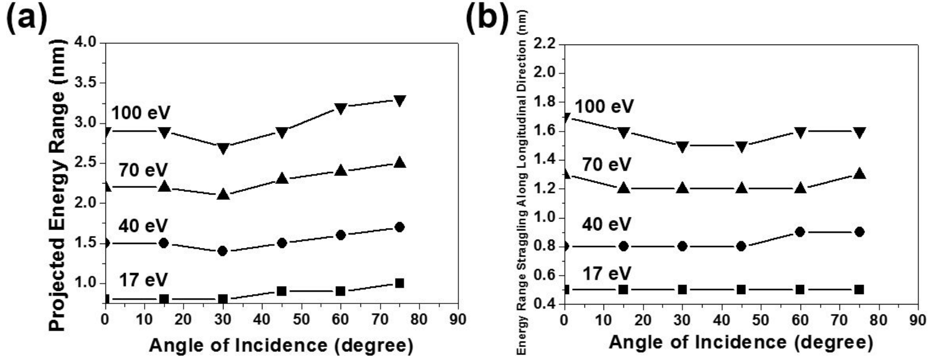

Figure. 3.16. (a) Projected energy range, *a*, and (b) energy range straggling along the longitudinal direction, *a*, with angle of ion incidence for an ion energy ranges of 17 - 100 eV.

Backscattered ion ratio, $R_{\text{b-s}}$, is calculated using the Monte Carlo simulation code TRIM [29] as shown in Fig. 3.17(a). Energy of backscattered ion is determined by the ratio of energy reflection coefficient and particle reflection coefficient [19] as shown in Fig. 3.17(b) which is follows:

$$E_{b-s}^{2nd} = \frac{\overline{E_{b-s}^{2nd}}}{E_i^{1st}} R_{b-s} E_i^{1st} \approx \frac{(1-\gamma)E_i^{1st}}{E_i^{1st}} R_{b-s} E_i^{1st} = (1-\gamma) R_{b-s} E_i^{1st} \tag{3.10}$$

Here, E_{b-s}^{2nd} is an energy of backscattered ion, γ is the ratio of energy transfer from incident ion and to carbon atoms in the graphite. The ratio of energy transfer from incident ion and to carbon atoms in the graphite is assumed as the averaged energy transfer for head-on collision as

$$\gamma = \frac{2M_1M_2}{(M_1+M_2)^2} \tag{3.11}$$

Here, M_1 and M_2 are the masses of incident ion and target atom, respectively. A flux of backscattered ion is determined by R_{b-s} as

$$\Gamma_{b-s}^{2nd} = R_{b-s}\Gamma_i^{1st} \tag{3.12}$$

Here, Γ_{b-s}^{2nd} is a flux of backscattered ion and Γ_i^{1st} is a flux of ininial ion.

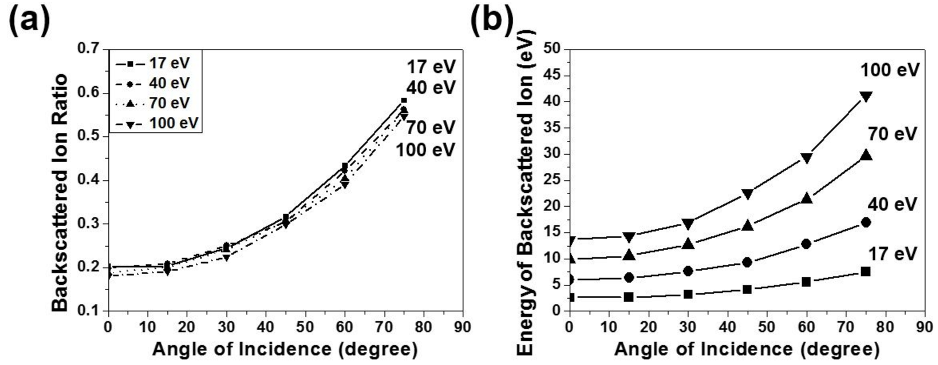

Figure. 3.17. (a) Backscattered ion ratio, and (b) energy of backscattered ion with angle of ion incidence for an ion energy ranges of 17 - 100 eV.

The total sputtering yield, Y_{tot}, can be expressed as follows:

$$Y_{tot} = Y_{phys}^{1st}(E_i^{1st},\sigma) + R_{b-s}Y_{phys}^{2nd}(E_{b-s}^{2nd},\pi-3\sigma) + Y_{chem}^{1st}(E_i^{1st},\Gamma_i^{1st},T_{surf}) + R_{b-s}Y_{chem}^{2nd}(E_{b-s}^{2nd},\Gamma_{b-s}^{2nd},T_{surf}) \tag{3.13}$$

Here, Y_{phys}^{2nd} is physical sputtering yield by incidence of

backscattered ion, Y_{chem}^{1st} is chemical sputtering yield by incidence of initial ion, Y_{chem}^{2nd} is chemical sputtering yield by incidence of backscattered ion, and T_{surf} is surface temperature. Calculated physical sputtering yield by incidence of initial ion, and chemical sputtering yield by backscattered ion with angle of ion incidence at an ion energy ranges of 17 – 100 eV are shown in Figs. 3.18(a) and (b), respectively.

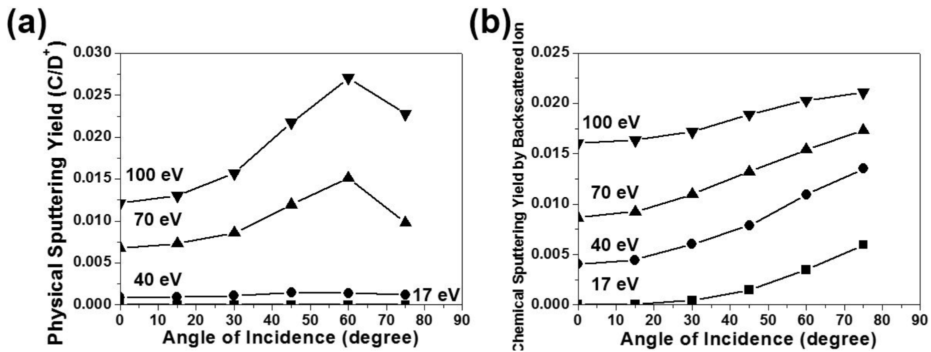

Figure. 3.18. (a) Physical sputtering yield by incidence of initial ion, and (b) chemical sputtering yield by backscattered ion with angle of ion incidence at an ion energy ranges of 17 – 100 eV.

According to the Fig. 3.17(b), an energy of backscattered ion is in the range of 2.6 – 41.3 eV, resulting in the averaged velocity range of 1.78×10^4 – 7.09×10^4 m/s [23]. Because the diameter and height of the conical tip is a few μm as shown in Figs. 3.13 and 3.14, time of flight for backscattered ion in a neutral form is ~0.1 msec. Residence time of neutral, which is the chamber

volume divided by pumping speed in an ECR chamber, is ~0.1 sec. Thousand difference between time of flight and residence time of neutral ensures that the collisions of backscattered ion are occurred. In particular, existence of collisions by backscattered ion can be a reason for the increment of the sputtering yield.

3.3.2. Increment of Sputtering Yield by Morphological Change of Graphite

Morphological changes of graphite after ion irradiation with energy range of 17 – 100 eV are shown in Fig. 3.19. Local angle of ion incidence, σ, is assumed as ~0, 45, 60, and 60 degrees with the ion energies of 17, 40, 70, and 100 eV, respectively, from the graphite morphologies as shown in Fig. 3.19. Physical, chemical and total sputtering yields of graphite in Eq. (3.13) from Roth model for plane surface and modified model for conical shaped surface with ion energy range of 17 – 100 eV are summarized in Table. 3.1. Physical sputtering yield by incidence of initial ion, Y_{phys}^{1st}, is increased with an energy of ion as expected by Roth [8]. Increase of local angle of ion incidence due to the morphological change of graphite with an energy of ion increases the increment of Y_{phys}^{1st} from Roth model for plane surface as shown in Fig. 3.20(a). It implies that the physical sputtering yield is more increased at the sharp tip, which provides large local angle of ion incidence. In addition, this increment can be increased with an energy of ion because aspect ratio of the conical tip is increased with an energy of ion. Physical sputtering yield by incidence of backscattered ion, $R_{b-s}Y_{phys}^{2nd}$, is almost negligible because an energy of backscattered ion is below 30 eV, even in high energy ion of 100

eV as shown in Fig. 3.17(b). Chemical sputtering yield by incidence of initial ion, Y_{chem}^{1st}, is same with Roth model because the chemical sputtering yield is not varied with local angle of ion incidence. However, chemical sputtering yield by incidence of backscattered ion, $R_{b-s} Y_{chem}^{2nd}$, is increased with an energy of ion because the backscattered ion ratio, R_{b-s}, an energy of backscattered ion, E_{b-s}^{2nd}, and a flux of backscattered ion, Γ_{b-s}^{2nd}, are increased with the local angle of ion incidence, i.e., aspect ratio of the conical tip. Thus, increase of additional collisions by backscattered ion increases the increment of chemical sputtering yield from Roth model for plane surface as shown in Fig. 3.20(b).

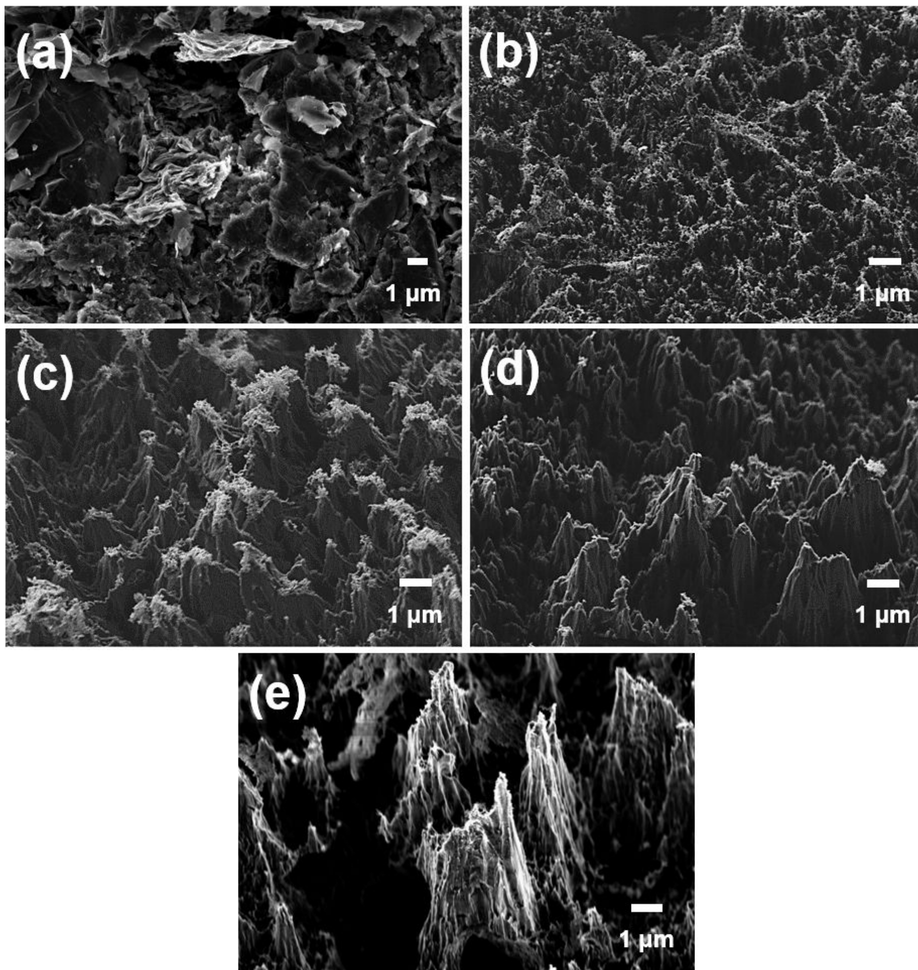

Figure. 3.19. Thirty degrees tilted SEM images of graphite (a) before and (b)-(e) after ion irradiation at a constant ion flux of 2.7×10^{17} $cm^{-2}s^{-1}$ and a dose of ion is 9.5×10^{20} cm^{-2}. Ion energies are (b) 17 eV, (c) 40 eV, (d) 70 eV, and (e) 100 eV.

	Roth model				Modified model			
	17 eV	**40 eV**	**70 eV**	**100 eV**	**17 eV**	**40 eV**	**70 eV**	**100 eV**
Y^{1st}_{phys}	**0**	**0.00087**	**0.00676**	**0.01208**	**0**	**0.00148**	**0.01515**	**0.02707**
$R_{b-s}Y^{2nd}_{phys}$	**0**	**0**	**0**	**0**	**0**	**0**	**0**	**0.00001**
Y^{1st}_{chem}	**0.01355**	**0.01806**	**0.01531**	**0.01234**	**0.01355**	**0.01806**	**0.01531**	**0.01234**
$R_{b-s}Y^{2nd}_{chem}$	**0**	**0**	**0**	**0**	**0**	**0.00241**	**0.00622**	**0.00756**
Y_{tot}	**0.01355**	**0.01893**	**0.02207**	**0.02442**	**0.01355**	**0.02195**	**0.03668**	**0.04698**

Table. 3.1. Physical, chemical and total sputtering yields of graphite in eq. (3.13) from Roth model for plane surface and modified model for conical shaped surface with an ion energy range of 17 – 100 eV at a constant ion flux of 2.7 × 10^{17} $cm^{-2}s^{-1}$.

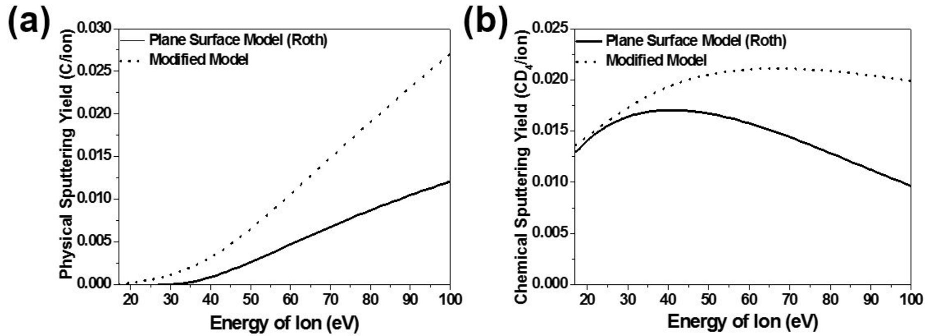

Figure. 3.20. (a) Physical and (b) chemical sputtering yields of graphite with an ion energy range of 17 – 100 eV. Plane surface model (Roth) represents the sputtering yield for plane surface and modified model represents the sputtering yield for conical tip.

Figure 3.21 shows the total sputtering yields of graphite with energy of ion from the Roth model for plane surface, modified model for conical shaped surface, and measured values by weight loss method. The measured sputtering yields by weight loss method are ~2 times larger than sputtering yields from the Roth model for plane surface. The sputtering yields from the modified model which considers the graphite morphology are close to the measured values by weight loss method, especially for the high energy ion incidence where the conical tips on the graphite are clearly generated. This implies that the graphite surface does not maintain its pristine surface as a plane surface which causes the increment of sputtering yield. As a result of this, carbon impurity influx into the deuterium plasma will be increased with operation condition, especially operation time. This can be the source of the spatially and temporally varying deuterium plasma properties of which details are discussed in the following section.

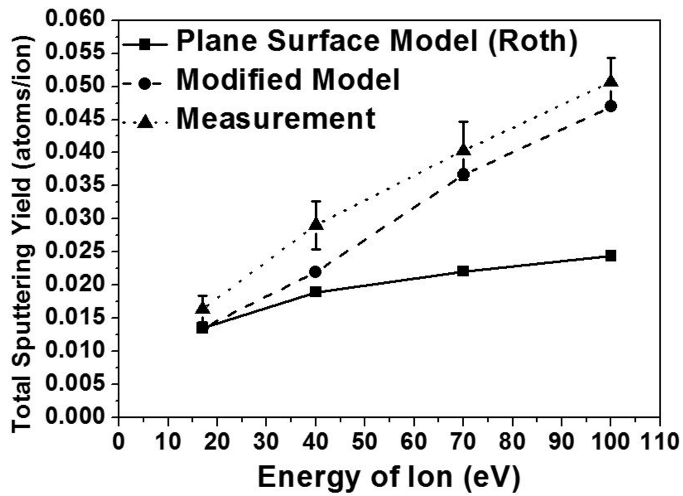

Figure. 3.21. Total sputtering yields of graphite with an ion energy range of 17 - 100 eV. Plane surface model (Roth) represents the sputtering yield for plane surface, modified model represents the sputtering yield for conical tip, and measurement represents the sputtering yield by weight loss method.

Chapter 4. Variation of Deuterium Plasma Properties by Carbon Impurity

4.1. Global Model for Spatially Averaged Deuterium Plasma Properties

The increment of sputtering yield by the morphological change of graphite facing deuterium plasma was discussed in Chapter 3. Because the carbon impurity influx is defined by the product of the sputtering yield and an ion flux as Eq. (1.1), the increment of the carbon impurity influx owing to the morphological change of graphite is expected. To investigate the variation of deuterium plasma properties owing to the carbon impurity influx, a reaction mechanism between the carbon impurity and deuterium plasma should be analyzed. In particular, the effect of the carbon impurity influx on the variation of deuterium plasma properties should be quantitatively analyzed. In order to approach this subject, a spatially averaged (global) model has been developed to analyze the interaction between the carbon impurity and deuterium plasma, and to compare with the experimental measurement. The direction of deuterium plasma property variation is estimated by extrapolation from its rate of change.

In the global model for D_2/CD_4 plasma, H_2 and CH_4 cross-section data are used instead of those for D_2 and CD_4 due to the lack of deuterium reaction cross-section data at a low temperature plasma. Because the cross-sections of hydrogen isotopes are similar to each other [43], the interaction between the D_2 plasma and CD_4 gas is similar to that between the H_2 plasma and CH_4 gas. The global model composed of balance equations for radical neutrals, neutrals, and ions, and then the power balance was formulated to consider the energy lost to the electron-neutral collision processes including ionization, excitation, and elastic collisions. Reactions in the ref. [44] are used in the model. Table 4.1 shows the considered nonradical neutrals, ions, radical neutrals, and sticking coefficients included in the model. Considered electron reactions with atoms and molecules, neutral - neutral reactions, and ion - neutral reactions are summarized in Tables 4.2, 4.3, and 4.4, respectively.

Nonradical neutrals	Ions	Radical neutrals	Sticking coefficient
D_2, CD_4, C_2D_2, C_2D_4, C_2D_6, C_3D_8	D^+, D_2^+, D_3^+, CD_3^+, CD_4^+, CD_5^+, $C_2D_2^+$, $C_2D_4^+$, $C_2D_5^+$	D, CD, CD_2, CD_3, C_2D_5	CD : 0.025, CD_2 : 0.025, CD_3 : 0.01, C_2D_5 : 0.01, D : 0.001

Table. 4.1. Ion species, neutral species and sticking coefficients [44] in the global model.

Reaction	Chemical reaction
CH_4, excitation	$e + CH_4 \rightarrow CH_4^* + e$
CH_4, ionization	$e + CH_4 \rightarrow CH_4^+ + 2e$
CH_4, ionization	$e + CH_4 \rightarrow CH_3^+ + H + 2e$
CH_4, dissociation	$e + CH_4 \rightarrow CH_3 + H + e$
CH_4, dissociation	$e + CH_4 \rightarrow CH_2 + 2H + e$
H, ionization	$e + H \rightarrow H^+ + e$
H, excitation	$e + H \rightarrow H^* + e$
H_2, excitation	$e + H_2 \rightarrow H_2^* + e$
H_2, ionization	$e + H_2 \rightarrow H_2^+ + 2e$
H_2, dissociation	$e + H_2 \rightarrow 2H + e$
C_2H_4, excitation	$e + C_2H_4 \rightarrow C_2H_4^* + e$
C_2H_4, ionization	$e + C_2H_4 \rightarrow C_2H_4^+ + 2e$
C_2H_4, dissociation	$e + C_2H_4 \rightarrow C_2H_2 + 2H + e$
C_2H_2, excitation	$e + C_2H_2 \rightarrow C_2H_2^* + e$
C_2H_2, ionization	$e + C_2H_2 \rightarrow C_2H_2^+ + 2e$
C_2H_6, ionization	$e + C_2H_6 \rightarrow C_2H_6^+ + 2e$
C_2H_6, ionization	$e + C_2H_6 \rightarrow C_2H_5^+ + H + 2e$
C_2H_6, dissociation	$e + C_2H_6 \rightarrow C_2H_5 + H + e$
C_2H_6, dissociation	$e + C_2H_6 \rightarrow C_2H_4 + 2H + e$
C_2H_5, ionization	$e + C_2H_5 \rightarrow C_2H_5^+ + 2e$
C_2H_5, ionization	$e + C_2H_5 \rightarrow C_2H_4^+ + H + 2e$
C_2H_5, dissociation	$e + C_2H_5 \rightarrow C_2H_4 + H + e$
CH_2, ionization	$e + CH_2 \rightarrow CH_2^+ + 2e$
CH_2, dissociation	$e + CH_2 \rightarrow CH + H + e$
CH_3, ionization	$e + CH_3 \rightarrow CH_3^+ + 2e$
CH_3, dissociation	$e + CH_3 \rightarrow CH_2 + H + e$
CH_3, dissociation	$e + CH_3 \rightarrow CH + 2H + e$

Table. 4.2. Electron reactions with atoms and molecules. Rate coefficients are used in Ref. [44-51].

Reaction	Rate Constant k (cm^3s^{-1})
$H + CH_4 \rightarrow CH_3 + H_2$	$2.2\times10^{-20} T^3 \exp(-4045/T)$
$H + CH_3 \rightarrow CH_2 + H_2$	$1\times10^{-10} \exp(-7600/T)$
$H + CH_2 \rightarrow CH + H_2$	$1\times10^{-11} \exp(900/T)$
$H + C_2H_6 \rightarrow C_2H_5 + H_2$	$2.4\times10^{-15} T^{1.5} \exp(-3730/T)$
$H + C_2H_5 \rightarrow 2CH_3$	6×10^{-11}
$H + C_2H_5 \rightarrow C_2H_4 + H_2$	5×10^{-11}
$H + C_2H_4 \rightarrow C_2H_3 + H_2$	$9\times10^{-10} \exp(-7500/T)$
$H + C_2H_2 \rightarrow C_2H + H_2$	$1\times10^{-10} \exp(-14000/T)$
$CH_3 + CH_3 \rightarrow C_2H_6$	6×10^{-11}
$CH_3 + CH_3 \rightarrow C_2H_5 + H$	$5\times10^{-11} \exp(-6800/T)$
$CH_3 + CH_3 \rightarrow C_2H_4 + H_2$	$1.7\times10^{-8} \exp(-16000/T)$
$CH_3 + CH_2 \rightarrow C_2H_4 + H$	7×10^{-11}
$CH_3 + CH \rightarrow C_2H_3 + H$	5×10^{-11}
$CH_2 + CH_2 \rightarrow C_2H_4$	1.7×10^{-12}
$CH_2 + CH_2 \rightarrow C_2H_2 + H_2$	$2\times10^{-10} \exp(-400/T)$
$CH + CH_4 \rightarrow C_2H_4 + H$	1×10^{-10}
$CH + CH_2 \rightarrow C_2H_2 + H$	6.6×10^{-11}
$CH + CH \rightarrow C_2H_2$	2×10^{-10}
$C_2H_5 + CH_3 \rightarrow C_3H_8$	4.2×10^{-12}
$CH + C_2H_6 \rightarrow C_3H_8$	4×10^{-10}

Table. 4.3. Neutral - neutral reactions. Rate coefficients are used in Ref. [44, 52-55] and T is the gas temperature.

Reaction	Rate Constant k (cm^3s^{-1})
$CH_4^+ + CH_4 \rightarrow CH_5^+ + CH_3$	1.5×10^{-9}
$CH_4^+ + H_2 \rightarrow CH_5^+ + H$	3.3×10^{-11}
$CH_3^+ + CH_4 \rightarrow CH_4^+ + CH_3$	1.36×10^{-10}
$H_2^+ + H_2 \rightarrow H_3^+ + H$	2.5×10^{-9}
$CH_3^+ + CH_4 \rightarrow C_2H_5^+ + H_2$	1.2×10^{-9}
$H_3^+ + C_2H_6 \rightarrow C_2H_5^+ + 2H_2$	2.0×10^{-9}
$H_3^+ + CH_4 \rightarrow CH_5^+ + H_2$	1.6×10^{-9}
$H_3^+ + C_2H_4 \rightarrow C_2H_5^+ + H_2$	1.9×10^{-9}
$H_3^+ + C_2H_2 \rightarrow C_2H_3^+ + H_2$	1.94×10^{-9}
$C_2H_2^+ + CH_4 \rightarrow C_2H_3^+ + CH_3$	4.1×10^{-9}
$C_2H_2^+ + CH_4 \rightarrow C_3H_4^+ + H_2$	6.25×10^{-10}
$C_2H_2^+ + CH_4 \rightarrow C_3H_5^+ + H$	1.44×10^{-9}
$C_2H_4^+ + C_2H_4 \rightarrow C_3H_5^+ + CH_3$	3.9×10^{-10}
$C_2H_4^+ + C_2H_4 \rightarrow C_4H_8^+$	4.3×10^{-10}
$CH_5^+ + C_2H_6 \rightarrow C_2H_5^+ + H_2 + CH_4$	5.0×10^{-10}
$C_2H_4^+ + C_2H_6 \rightarrow C_3H_6^+ + CH_4$	2.03×10^{-13}
$C_2H_4^+ + C_2H_6 \rightarrow C_3H_7^+ + CH_3$	1.32×10^{-11}
$C_2H_5^+ + C_2H_2 \rightarrow C_4H_7^+$	6.7×10^{-10}
$C_2H_5^+ + C_2H_4 \rightarrow C_3H_5^+ + CH_4$	3.1×10^{-10}
$C_2H_5^+ + C_2H_4 \rightarrow C_4H_9^+$	3.0×10^{-10}

Table. 4.4. Ion – neutral reactions. Rate coefficients are used in Ref. [44, 55-58].

The electron energy distribution function (EEDF) is assumed as Maxwellian which is expressed as

$$f(\varepsilon)=\frac{1}{\left(kT_e\right)^{3/2}}\frac{2}{\sqrt{\pi}}\varepsilon^{1/2}\exp\left(-\frac{\varepsilon}{kT_e}\right) \tag{4.1}$$

Here, ε is the electron energy. The overall charge neutrality

$$\sum_i n_i = n_e \tag{4.2}$$

is implied with the assumption of singly charged ion species. Here, n_i is the ion density.

The set of balance equations is established for deuterium,

$$\frac{\partial n_{D_2}}{\partial t} = I_{D_2} - O_{D_2} - \sum_i k_i n_e n_{D_2} + \sum_{jkm} k_j n_k n_m - \sum_{ls} k_l n_s n_{D_2} + 0.5 K_{wall}^{D} n_D \tag{4.3}$$

deuterated methane (CD_4),

$$\frac{\partial n_{CD_4}}{\partial t} = I_{CD_4} - O_{CD_4} - \sum_i k_i n_e n_{CD_4} + \sum_{jkm} k_j n_k n_m - \sum_{ls} k_l n_s n_{CD_4} \tag{4.4}$$

and other radical and nonradical neutral species,

$$\frac{\partial n_r}{\partial t} = \sum_h k_h n_e n_h + \sum_{jkm} k_j n_k n_m - \sum_{ls} k_l n_s n_r - K_{wall}^{r} n_r - O_r \tag{4.5}$$

Here, I_{D2}, I_{CD4} are the inflow, O_{D2}, O_{CD4}, and O_r are the outflows of the D_2, CD_4, and other radical and nonradical neutral species r per unit time, respectively, k is the rate constant, and K_{wall} is the number of species gain or lost on the walls per unit time and unit volume as a result of the surface reactions. Inflow of D_2 is I_{D2}[cm^{-3}/s] $\approx$ 4.4 $\times$ 10^{17} J_{D2} [sccm]/V where J_{D2} is deuterium gas inlet flow rate and V is the chamber volume in cm^3. Inflow of CD_4 is

$$I_{CD_4} = Y \Gamma_{D+} \frac{A_{graphite}}{V} \tag{4.6}$$

Here, Y is the sputtering yield of graphite. The sputtering of

graphite is considered as formation of CD_4. Outflow of species is $O = \upsilon_{pump} n/V$ where υ_{pump} is the pumping rate in cm^3/s. Number of species gain or lost on the walls is $K_{wall} = \gamma \upsilon_{thr} S_{surf}/4V$ where γ is the wall sticking coefficient, υ_{thr} is the average thermal velocity of species, and S_{surf} is the chamber surface area.

The balance equations for the ion species is

$$Vn_e \nu_{iz,i} = (h_L A_L + h_R A_R) n_i u_{B,i} + V \sum_{j=1}^{N_s} k_{cx,ij} n_i n_j \approx (h_L A_L) n_i u_{B,i} + V \sum_{j=1}^{N_s} k_{cx,ij} n_i n_j \quad (4.7)$$

Here, $\nu_{iz,i}$ is the ionization frequency for the production of ion species, h_L and h_R are the ratios of the densities of ion species on the axial and radial directions to the bulk, respectively, A_L and A_R are the areas of axial and radial directions, respectively, $u_{B,i}$ is the ion Bohm velocity, and the k_{cx} is the charge-exchange rate coefficient. The strong axial magnetic field of the ECR plasma suppresses the radial diffusion of the plasma [23].

The power balance equation is

$$P_{in} = P_{ev} + P_w \quad (4.8)$$

Here, P_{in} is the total power deposited to the plasma. The energy lost to the electron-neutral collision processes is

$$P_{ev} = en_e V \sum_{i=1}^{q} \nu_{iz,i} \varepsilon_{L,i} = en_e V \sum_{i=1}^{q} \left(\nu_{iz,i} \varepsilon_{iz,i} + \sum_{k=1}^{N_{exc}} \nu_{exc,k} \varepsilon_{exc,k} + 3 \nu_{elas} m_e T_{eff} / M_i \right) \quad (4.9)$$

Here, ε_L is the total collisional energy loss for the production of the electron-ion pair, ε_{iz} is the threshold ionization energy for the production of ion species, ν_{exc} is the excitation frequency, ε_{exc} is

the threshold excitation energy, ν_{elas} is the elastic collision frequency, and T_{eff} is the effective electron temperature. The energy lost to the loss of kinetic energy of charged species on the walls is

$$P_w \approx \sum_{i=1}^{g} e n_i v_{B,i} (h_L A_L)(\varepsilon_{e\omega} + \varepsilon_{i\omega}) \tag{4.10}$$

Here, $\varepsilon_{e\omega}$ and $\varepsilon_{i\omega}$ are the mean electron kinetic energy lost per electron and the sum of energy gained by the ion as it traverses the sheath, respectively.

Because the inflow of deuterated methane (CD_4) is determined as equation (4.6), calculation of the sputtering yield is necessary to estimate the carbon impurity influx. According to the morphological change of graphite as discussed in the Chapter 3.2, the sputtering yield is calculated by using the modified sputtering yield model as discussed in the Chapter 3.3. Deuterated methane (CD_4) which is caused by the sputtering of graphite facing deuterium ion irradiation reacts with deuterium plasma, resulting in the formation of various deuterated carbon species. Figure 4.1 shows the neutral densities of deuterium and deuterated carbon species (C_xD_y) by the global model. Because the sputtering of graphite is considered as formation of CD_4, a neutral density of CD_4 is largest in comparison with other deuterated carbons. In addition, increases of deuterated carbon densities are expected as the sputtering yield was increased. The increment of deuterated carbon densities by the sputtering of graphite can also be

estimated by the measurement of the partial pressure of CD_4, which is measured by RGA as shown in Fig. 4.2. For an incident ion energy of 17 eV, the partial pressure of CD_4 is almost constant with a little increase at the end of the operation time. For an incident ion energy of 40 eV, the increase of partial pressure of CD_4 with operation time is observed. For an incident ion energy of 100 eV, the rapid increase of partial pressure of CD_4 is observed at the early ion irradiation period, and the slow increase is observed at the end of the operation time. This result can be explained that the morphological change of graphite is remarkable with energy of ion, which corresponds to the results in the Chapter 3.2.

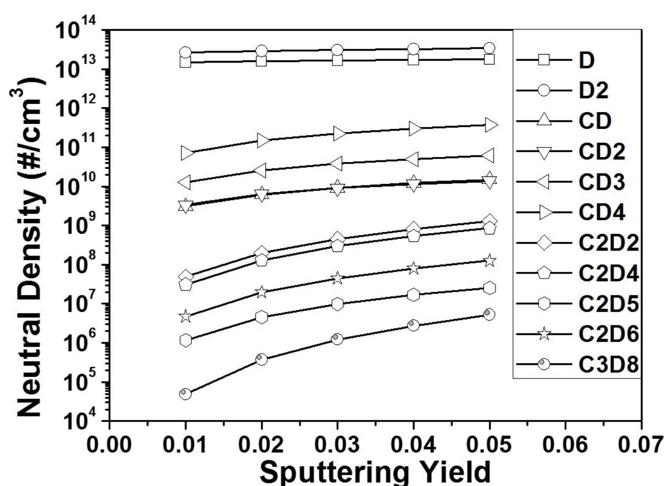

Figure. 4.1. Computed neutral densities of deuterium and deuterated carbon species by the global model with microwave power of 400 W and an ion energy of 40 eV.

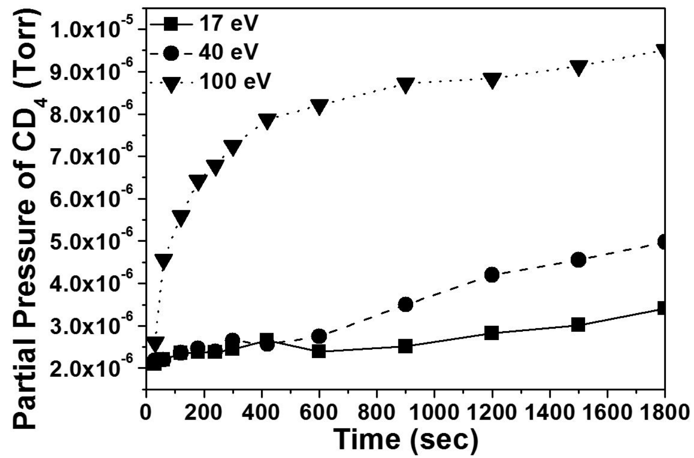

Figure. 4.2. Partial pressure of deuterated methane (CD_4) with operation time for an incident ion energy range of 17 – 100 eV in an ECR chamber. A deuterium gas pressure of 1 mTorr and microwave power of 400 W are maintained in the whole operation time.

4.2. Spatially Varying Deuterium Plasma Properties by Carbon Impurity

4.2.1. Decrease of Electron Temperature and Increase of Electron Density in Space

Figure 4.3 shows the measured electron temperature and electron density for a stainless steel target and a graphite target with axial distance from the target in an ECR chamber at microwave power of 400 W. Plasma properties were measured after 20 minutes from the ignition. A stainless steel target was chosen for comparison with a graphite target because the secondary electron coefficients of two materials are almost same [59], and there is no carbon by-product at a stainless steel target. An electron temperature for a graphite target is lower than that for a stainless steel target, and an electron density for a graphite target is higher than that for a stainless steel target. Because the operation conditions such as deuterium pressure, coil current, microwave power, and ion energy are constant, different types of target cause this spatially varying deuterium plasma properties. Rate coefficients of dissociation and ionization of deuterated methane (CD_4) are larger than those for deuterium (D_2), respectively [42] as shown in Fig. 4.4. Thus, formation of carbon (C) and deuterated methane (CD_4) by physical and

chemical sputtering, respectively, causes the decrease of an electron temperature and the increase of an electron density. For an ion energy of 17 eV, differences in the spatial variation of deuterium plasma properties are shown within ~60 mm from the target. Because the carbon impurity is generated at the surface of a graphite target, variation region is more focused near a graphite target. For an ion energy of 40 eV, differences in the spatial variation of deuterium plasma properties are shown in the whole area of plasma, i.e. bulk plasma. Thus, the bulk plasma properties can be varied by the increase of the carbon impurity influx, and this will be discussed in detail in following section.

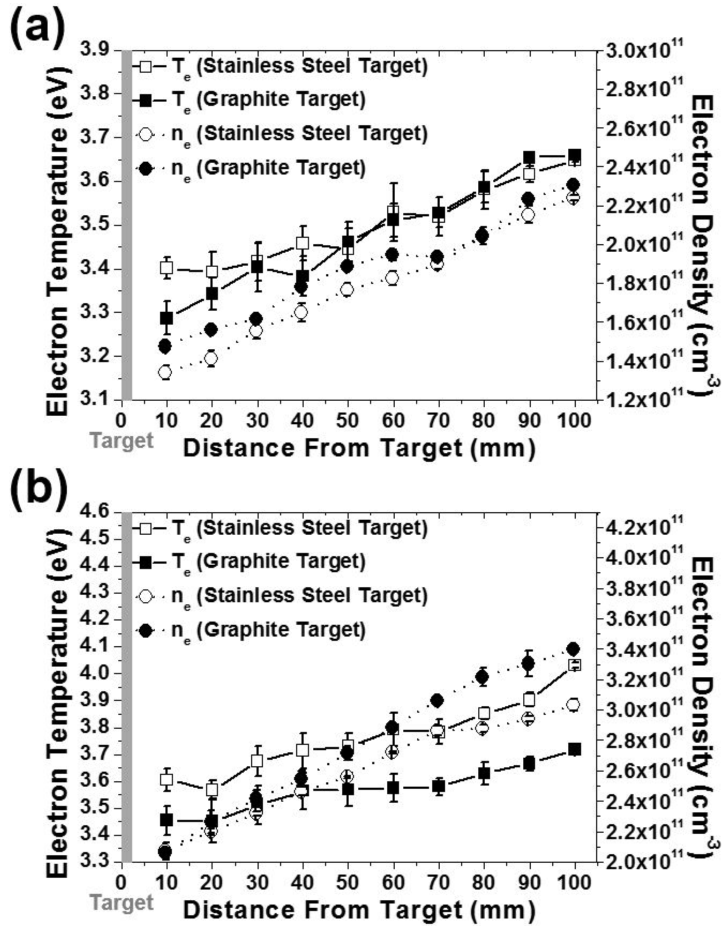

Figure. 4.3. Measured electron temperature (square with solid line) and electron density (circle with dotted line) with distance from the target in an ECR chamber at an ion energy of 100 eV and microwave power of 400 W. Empty symbol: stainless steel target; filled symbol: graphite target. Ion energies are (a) 17 eV and (b) 40 eV.

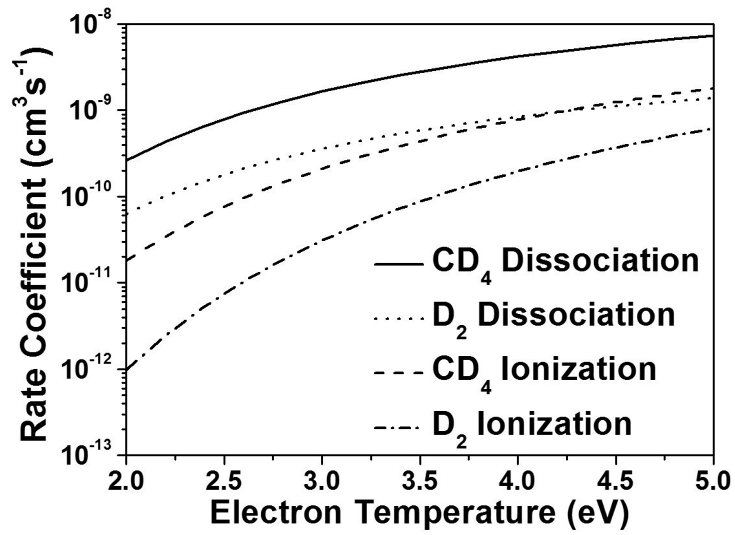

Figure. 4.4. Rate coefficients of dissociation and ionization of deuterated methane (CD_4) and deuterium (D_2).

4.2.2. Bulk Plasma Variation by Increased Carbon Impurity Influx

The increase of deuterated methane (CD_4) with an energy of ion was shown in Fig. 4.2 and the possibility of the bulk plasma variation was shown in Fig. 4.3. Figure 4.5 shows the measured electron temperatures and electron densities for a graphite target, which are normalized by those for a stainless steel target in an ECR chamber. For an ion energy of 40 eV, the decrease of an electron temperature and the increase of an electron density are intensified with axial distance from the target in comparison with those for an ion energy of 17 eV. All carbon impurities do not ionized in the plasma near the target when the sputtering yield is increased, i.e., an ion energy is increased. This causes the penetration of the carbon impurities into the bulk plasma where an electron temperature is higher than that for the plasma near the target. Thus, dissociation and ionization of deuterated carbon are more occurred in the bulk plasma.

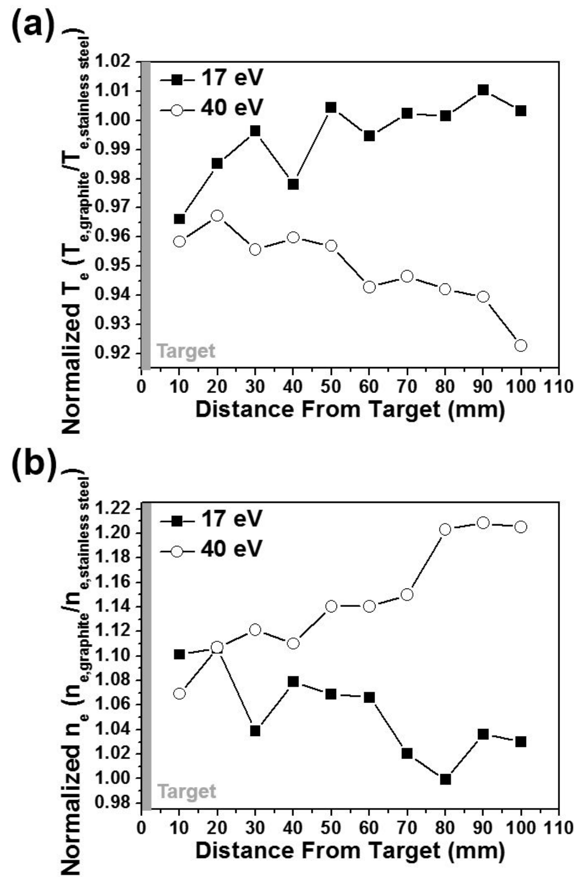

Figure. 4.5. (a) Measured electron temperatures and (b) electron densities for a graphite target which are normalized by those for a stainless steel target in an ECR chamber at microwave power of 400 W.

Figure 4.6 shows the computed and measured electron temperatures and electron densities with sputtering yield at an ion energy of 40 eV. Computed values are calculated by the global model which was explained in the Chapter 4.1. Those data

show similar trend within ~10 % differences in absolute values. This indicates that the increase of sputtering yields causes the decrease of an electron temperature and the increase of an electron density in the space. This also indicates that the variation of the deuterium plasma properties is caused by the carbon impurity influx. This shows that the bulk plasma, which is relatively far from a graphite target, can be affected by the carbon impurity from graphite. Thus, there is a possibility that the bulk plasma properties are affected by wall condition. If the previous sputtering yield model for a plane surface is used, variation widths of the plasma properties are underestimated ~35 %. In other words, the consideration of the morphological change of graphite is necessary to analyze, and to estimate the variation of deuterium plasma properties.

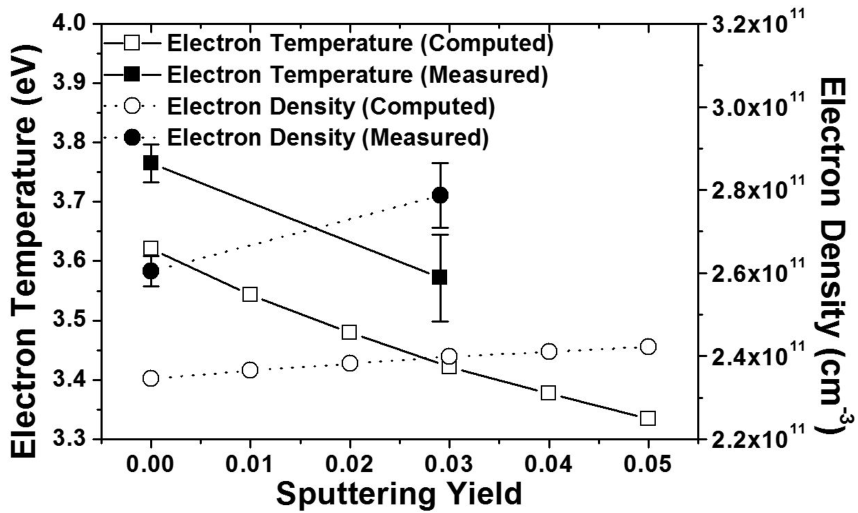

Figure. 4.6. Computed and measured electron temperatures (square with solid line) and electron densities (circle with dotted line) with sputtering yield at an ion energy of 40 eV. Empty symbol: computed values; filled symbol: measured values. Measured values are positioned at sputtering yields of 0 and 0.029 for stainless steel target and graphite target, respectively.

4.3. Temporally Varying Deuterium Plasma Properties by Carbon Impurity

4.3.1. Decrease of Electron Temperature and Increase of Electron Density with Operation Time

Spatially varying deuterium plasma properties were analyzed in Chapter 4.2. As a result of the morphological change of graphite by deuterium plasma irradiation, increased sputtering yield causes the variation of bulk plasma properties. Because the graphite morphology is also changed as operation time is increased, temporally varying deuterium plasma properties can be caused by temporally varying graphite morphology. Figure 4.7(a) shows the measured electron temperature and electron density with operation time for an ion energy of 40 eV, which are obtained from the average of the measured probe data in an ECR source. For a stainless steel target, an electron temperature and an electron density are almost unchanged with operation time. For a graphite target, however, sudden decrease of an electron temperature and increase of an electron density are observed in 5 min, and then both stabilize. This indicates that the morphological change of graphite is remarkable within 5 min, and this variation may be closely related to the formation of deuterated methane (CD_4), which are similar to the variations of

plasma property as observed in the H_2 plasma with inflow of CH_4 [22]. The effect of CD_4 addition on the bulk plasma property is evaluated by using the global model, which contains the energy lost to the electron-neutral collision processes. Figure 4.7.(b) shows the comparison of the computed and measured electron temperatures and electron densities for a graphite target with sputtering yield at an ion energy of 40 eV. Those data show similar trend within ~8 % differences in absolute values. This indicates that the increase of sputtering yields causes the decrease of an electron temperature and the increase of an electron density. In particular, it provides that the variation of deuterium plasma properties is influenced dominantly by the inflow of CD_4.

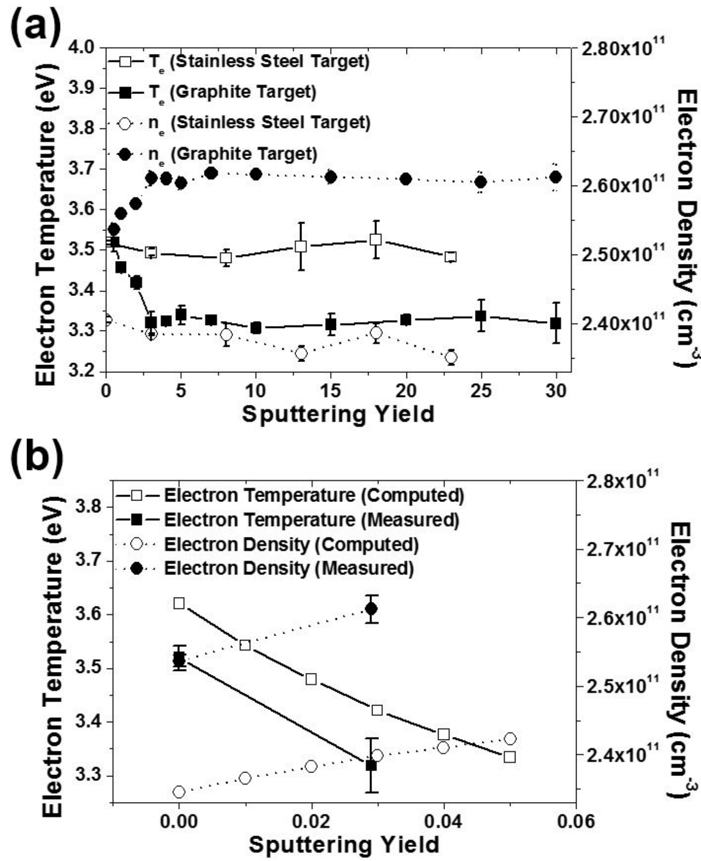

Figure. 4.7. (a) Measured electron temperature (square with solid line) and electron density (circle with dotted line) with operation time in an ECR chamber at an ion energy of 40 eV. Empty symbol: stainless steel target; filled symbol: graphite target. (b) Computed and measured electron temperatures (square with solid line) and electron densities (circle with dotted line) with sputtering yield at an ion energy of 40 eV. Empty symbol: computed values; filled symbol: measured values. Measured values are positioned at sputtering yields of 0 and 0.029 for operation times of 0 and 1800 sec, respectively.

Figure 4.8 show the measured electron temperature and electron density for a graphite target with operation time at a constant ion energy of 100 eV, and microwave powers of 400 and 600 W. The decrease of an electron temperature and the increase of an electron density with operation time are more remarkably observed than those in Fig. 4.7. In addition, the decrease of an electron temperature and the increase of an electron density are observed in 15 min, and then both stabilize. This indicates that the morphological change of graphite is remarkable within 15 min because the severe morphological changes are expected in a high energy ion incidence. It notes that the variation of deuterium plasma properties at an ion energy of 40 eV is observed in 5 min as shown in Fig. 4.7. When microwave power is increased to 600 W in comparison with 400 W, the variation depth of an electron density and the saturation time are larger than those for 400 W, respectively. A high ion flux causes severe changes of the graphite morphology, resulting in the incrementing of the carbon impurity influx and variation of deuterium plasma properties. This will be interpreted in detail in following section.

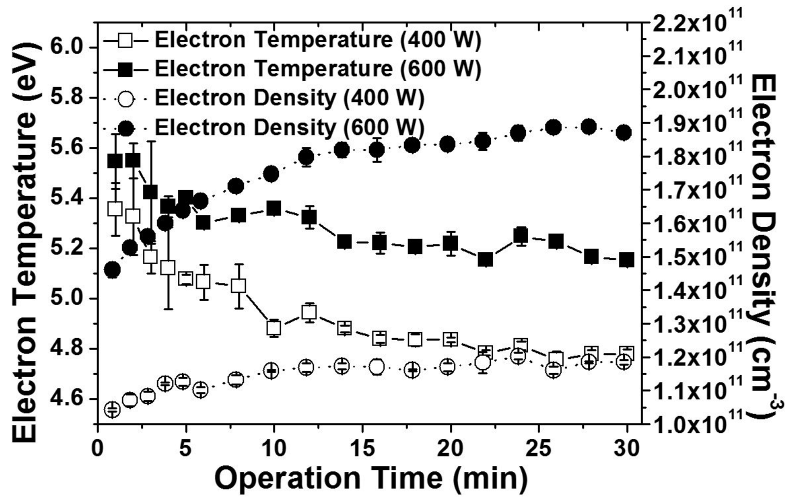

Figure. 4.8. Measured electron temperature (square with solid line) and electron density (circle with dotted line) with operation time in an ECR chamber at an ion energy of 100 eV. Empty symbol: microwave power of 400 W; filled symbol: microwave power of 600 W

4.3.2. Intensified Variation of Plasma Properties by Graphite Morphology

Figure 4.9 shows normalized electron density, which is divided by an electron density at operation time of 0 min, with operation time in an ECR chamber at ion energies of 40 and 100 eV and microwave powers of 400 and 600 W. Graphite morphologies for an ion energy of 40 eV and microwave power of 400 W, an ion energy of 100 eV and microwave power of 400 W, and an ion energy of 100 eV and microwave power of 600 W are shown in Figs. 3.8(a), 3.8(c), and 3.9(b), respectively. Variation width and time for saturation of the normalized electron density for an ion energy of 40 eV and microwave power of 400 W are ~3 % and ~3 min, respectively. When an ion energy is increased to 100 eV, variation width and time for saturation of normalized electron density are increased to ~15 % and ~10 min, respectively. In addition, variation width and time for saturation of normalized electron density are increased to ~30 % and ~15 min at microwave power of 600 W, respectively. Thus, severe changes of the graphite morphology by high energy and flux of ion incidence, i.e., the energy dose, cause the large increment of the carbon impurity influx, resulting in large variation of an electron density.

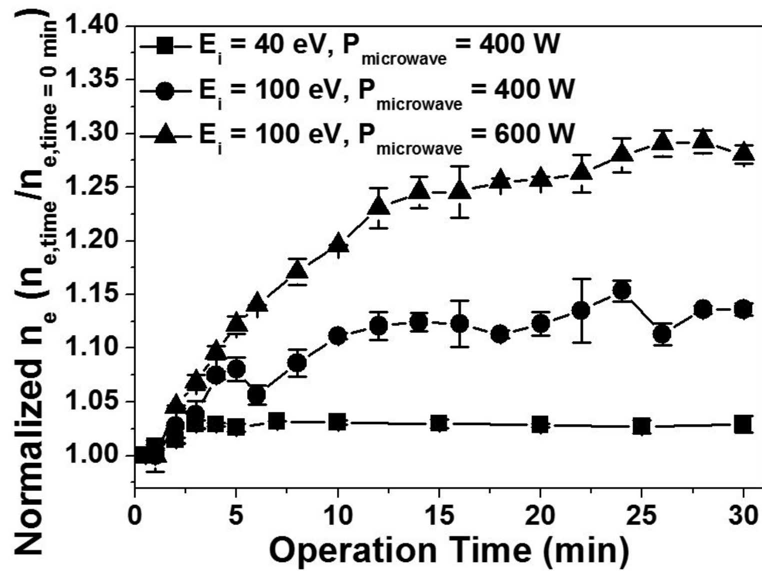

Figure. 4.9. Electron density which is divided by an electron density at operation time of 0 min with operation time in an ECR chamber at ion energies of 40 and 100 eV and microwave powers of 400 and 600 W.

Chapter 5. Re-Increment Mechanism of Carbon Impurity Formation by Increase of Ion Flux

The variation of deuterium plasma properties by the carbon impurity was discussed in Chapter 4. As shown in Fig. 1.2(b) and discussed in Chapter 1.3, the flowed carbon impurity changes the deuterium plasma properties, especially the electron temperature and electron density, resulting in the variation of the ion flux, Γ_i^1, on the surface. Because an ion flux is increased with operation time as shown in Fig. 5.1(a), the effect of the increased ion flux on the incrementing of the sputtering yield, i.e., re-increment of the sputtering yield, should be evaluated. In addition, surface temperatures of graphite are more increased with operation time due to the increased ion flux as shown in Fig. 5.1(b). Increases of both an ion flux and surface temperature are expected to increase the chemical sputtering yield by additional collisions of backscattered ion as shown Eq. (3.13).

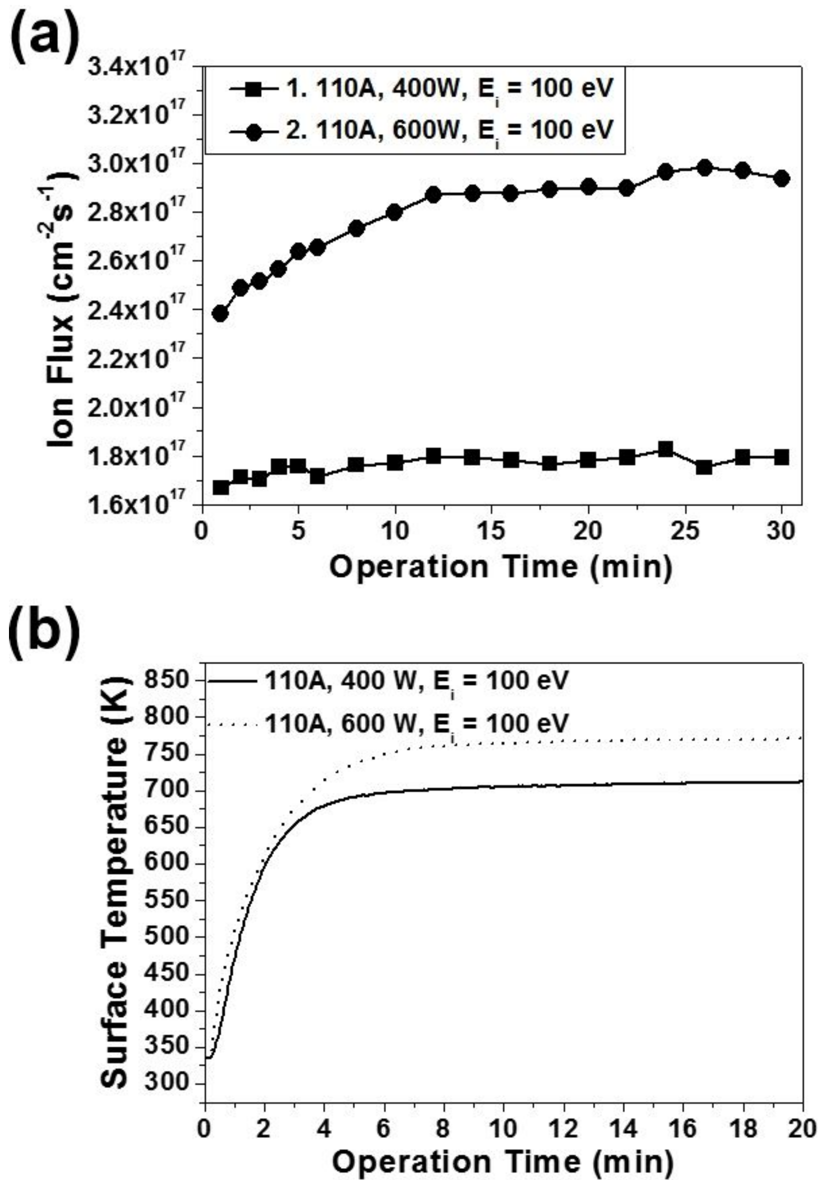

Figure. 5.1. (a) Ion flux and (b) surface temperature of graphite with operation time for microwave powers of 400 and 600 W at a constant coil current of 110 A and an ion energy of 100 eV.

As expected in the sputtering yield formula in Eqs. (3.12) and (3.13), chemical sputtering yields by initial ion and backscattered ion depend on the initial ion flux and backscattered ion flux, respectively. The local angle of ion incidence, σ, is assumed as ~60 and 67.5 degrees with microwave powers of 400 and 600 W, respectively, from the graphite morphologies as shown in Fig. 5.2. Larger local angle of ion incidence provides larger backscattered ion ratio than lower one. Thus, the product of backscattered ion ratio (R_{b-s}) and chemical sputtering yield by incidence of backscattered ion (Y_{chem}^{2nd}) for the Fig. 5.2(a) is larger than that for the Fig. 5.2(b) as shown in Fig. 5.3(a). Thus, the total sputtering yield with operation time for the Fig. 5.2(a) is also larger than that for the Fig. 5.2(b) as shown in Fig. 5.3(b). Figure 5.4 shows the total sputtering yields of graphite with microwave power from the Roth model for a plane surface, modified model for a conical shaped surface, and measured values by weight loss method. The measured sputtering yields by weight loss method are ~2 times larger than sputtering yields from the Roth model for a plane surface. The sputtering yields from the modified model, which considers the increment of $R_{b-s}Y_{chem}^{2nd}$, are close to the measured values by weight loss method. This indicates that the variation of the deuterium plasma properties caused by the carbon impurity influx can accelerate graphite wall erosion. Consequently, the consideration of

variations in both the graphite morphology and deuterium-plasma properties is essential in order to understand the interaction between deuterium plasma and a graphite surface.

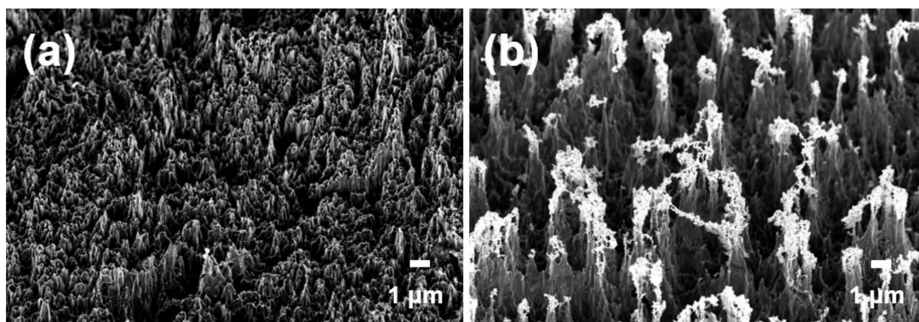

Figure. 5.2. Thirty degrees tilted SEM images of graphite after ion irradiation at a constant ion energy of 100 eV. Microwave powers of (a) 400 W and (b) 600 W.

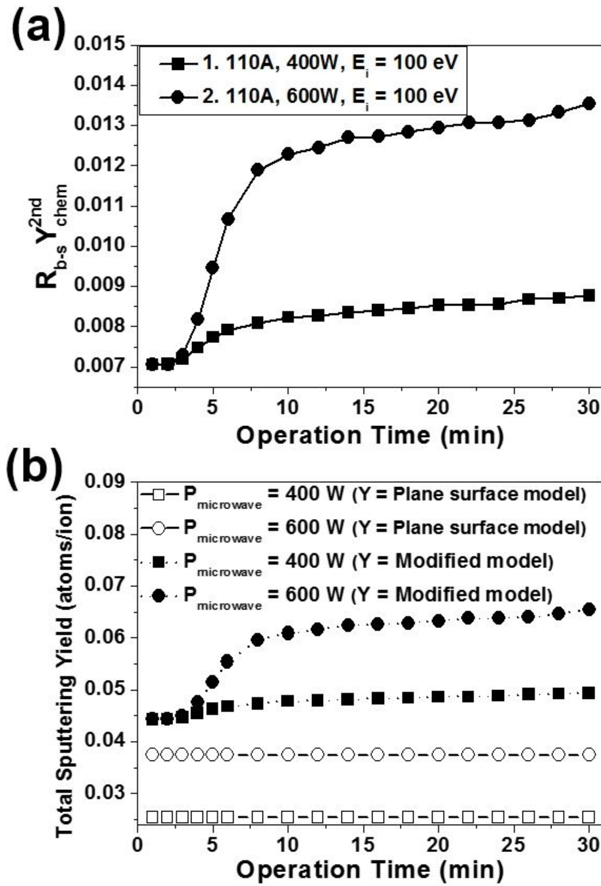

Figure. 5.3. (a) The product of backscattered ion ratio and chemical sputtering yield by incidence of backscattered ion, and (b) total sputtering yield with operation time at a constant coil current of 110 A, an ion energy of 100 eV, and microwave powers of 400 W and 600 W.

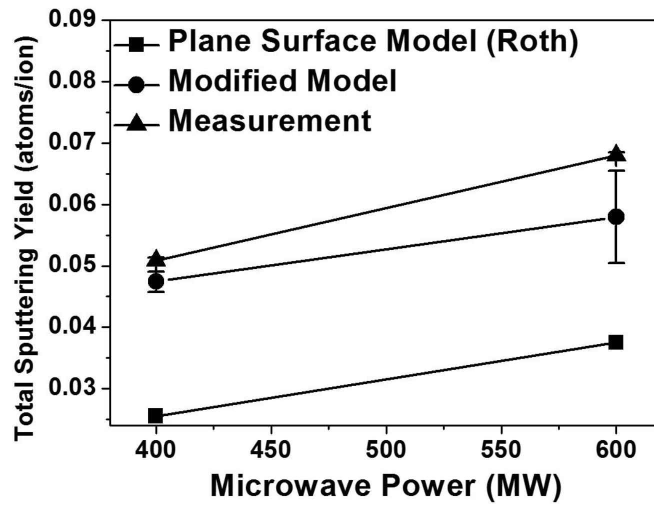

Figure. 5.4. Total sputtering yields of graphite with an ion energy of 100 eV. Roth model represents the sputtering yield for plane surface and modified model represents the sputtering yield for conical tip.

Chapter 6. Conclusions

The deuterium plasma-graphite surface interaction is investigated by considering the surface morphology, which is a new perspective on interpreting plasma-surface interaction studies. The morphological change of graphite during the deuterium plasma irradiation is turned out to increase the carbon impurity influx into the deuterium plasma. The carbon impurity causes spatial and temporal variations of deuterium plasma properties, and these variations are further increased by the morphological change of graphite. Thus, the consideration of the surface morphology is found to be critical in the analysis of the plasma-surface interaction including the deuterium plasma-graphite surface interaction.

The degree of morphological change of graphite during the deuterium plasma irradiation is determined by both physical properties (i.e. the energy dose and sheath electric field) and chemical properties (i.e. C-D bond formation) of the plasma. As the energy of incident ions induces atomic motions in the graphite, the total energy transferred to the graphite per unit area, i.e., the energy dose, determines the degree of its morphological change. The formation of sheath on the graphite surface during the deuterium plasma irradiation, generates force, which is an interaction between the induced dipole and sheath

electric field, thereby shaping the graphite morphology. As the sheath potential and C-D formation determines the intensities of the sheath electric field and the induced dipole respectively, plasma properties are the important factors to be considered in the study of morphological change of graphite.

The morphological change of graphite has increased the sputtering yield by causing increase in both the local angle of incident ions and collisions of backscattered ions. The physical sputtering yield for the C formation and the chemical sputtering yield for the CD_4 formation, in particular, are increased with the morphological change of graphite. This indicates that the sputtering yields are determined by physical and chemical properties of the plasma, energy dose and the C-D bond formation respectively. Therefore, the levels of plasma irradiation determines the levels of the morphological change of graphite as well as the carbon impurity formation.

The variation of the deuterium plasma properties is turned out to be the decrease in electron temperatures and the increase in electron densities with an influx of the carbon impurity. Considering that the higher energy dose, the more severe morphological changes are found in the graphite, the range of the deuterium plasma variation is determined by the plasma irradiation conditions. The increase in ion flux due to the carbon impurity influx during deuterium plasma irradiation is the key reason for the re-increment of the sputtering yield. Therefore, the

consideration of variations in both the graphite morphology and deuterium plasma properties is essential in order to understand the deuterium plasma - graphite surface interaction.

The present study will contribute to the understanding of the KSTAR plasma, which uses deuterium plasma with graphite, and to the understanding of the plasma processing for carbon and hydrogen gases. In particular, a new discovery described here regarding that the by-product generated from plasma irradiation can lead to the temporal variation of the plasma properties is believed to be highly useful in the fields of studying estimation and control of plasma properties

References

[1] Suk-Ho Hong, Sang-Joon Park, Jae-Myung Choe, Young-Mu Jeon, Seung Jae Yang, Sun-Taek Lim, Sooseok Choi, Young-Gil Jin, Chong Rae Park, and Gon-Ho Kim, J. Nucl. Mater., **438** (2013) S698.

[2] C. H. Wu, J. P. Bonal, H. Kwast, F. Moons, G. Pott, H. Werle, and G. Vieider, Fusion Eng. Des. **39-40** (1998) 263.

[3] P. Paz, C. Garcia-Rosales, J. Echeberria, M. Balden, J. Roth, and R. Behrisch, Fusion Eng. Des. **56-57** (2001) 325.

[4] J. G. Bak, Y. S. Oh, H. S. Kim, S. H. Hahn, S. W. Yoon, Y. M. Jeon, W. W. Xiao, W. H. Ko, W. C. Kim, J. G. Kwak, H. J. Woo, K. S. Chung, and the KSTAR project team, Contrib. Plasma Phys., **53** (2013) 69.

[5] T. Yamashina and T. Hino, Appl. Surf. Sci., **48/49** (1991) 483.

[6] G. Federici and C.H. Wu, J. Nucl. Mater., **207** (1993) 62.

[7] A. Kirschner, V. Philipps, J. Winter, and U. Kögler, Nucl. Fusion, **40** (2000) 989.

[8] J. Roth, A. Kirschner, W. Bohmeyer, S. Brezinsek, A. Cambe, E. Casarotto, R. Doerner, E. Gauthier, G. Federici, S. Higashijima, J. Hogan, A. Kallenbach, H. Kubo, J. M. Layet, T. Nakano, V. Philipps, A. Pospieszczyk, R. Preuss, R. Pugno, R. Ruggiéri, B. Schweer, G. Sergienko, and M. Stamp, J. Nucl. Mater., **337-339** (2005) 970.

[9] D. Reiter, M. Baelmans, and P. Börner, Fusion Sci. Technol., **47** (2005) 172.

[10] R. A. Pitts, “Tokamak edge physics and plasma-wall interactions”, CEA/IRFM (2012) ITER_D_7AP2A9.

[11] S. Brezinsek, “Impurity seeding for heat flux control in JET”, 2014 ITPA Div/SOL meeting in Kanazawa.

[12] A.S. Kukushkin, "SOLPS Modelling of Ne and N seeding on ITER", 2014 ITPA Div/SOL meeting in Kanazawa.

[13] M. Groth, "EDGE2D/EIRENE simulations of nitrogen seeded JET baseline ELMy H-mode plasmas“, 2014 ITPA Div/SOL meeting in Kanazawa.

[14] M. Balden, E. de Juan Pardo, H. Maier, P. Starke, and U. Fantz, Phys. Scr. **T111** (2004) 123.

[15] M. J. Baldwin, R. P. Doerner, D. Nishijima, K. Schmid, D. G. Whyte, J. G. Kulpin, and G. Wright, J. Nucl. Mater. **358** (2006) 96.

[16] Seung Jae Yang, Jae-Myung Choe, Young-Gil Jin, Sun-Taek Lim, Kunsil Lee, Yern Seung Kim, Sooseok Choi, Sang-Joon Park, Y.S. Hwang, Gon-Ho Kim, and Chong Rae Park, Fusion Eng. Des. **87** (2012) 344.

[17] D. M. Goebel, J. Bohdansky, R. W. Conn, Y. Hirooka, B. Labombard, W. K. Leung, R. E. Nygren, J. Roth, and G. R. Tynan, Nucl. Fusion **28** (1988) 1041.

[18] Qiangmin Wei, Kun-Dar Li, Jie Lian, and Lumin Wang, J. Phys. D: Appl. Phys., **41** (2008) 172002.

[19] P. Stangeby: The Plasma Boundary of Magnetic Fusion Devices (IOP Publishing, Bristol, 2000).

[20] M. Küstner, W. Eckstein, V. Dose, and J. Roth, Nucl. Instr. and Meth. in Phys. Res. B **145** (1998) 320.

[21] J. G. Bak, "Study on the SOL width, particle and heat fluxes at divertor in KSTAR", 2014 ITPA Div/SOL meeting in Kanazawa.

[22] K. Hassouni, O. Leroy, S. Farhat, and A. Gicquel , Plasma Chem. Plasma Proc, **18** (1998) 325.

[23] M. A. Lieberman, A. J. Lichtenberg: Principles of Plasma Discharges and Materials Processing. 2nd ed. New York: John Wiley & Sons; 1994.

[24] BongJu Lee, David Hill, K. H. Im, L. Sevier, Jung-Hoon Han, and Bastiaan J. Braams, Fusion Sci. Technol., **37** (2000) 110.

[25] A. A. Airapetov, L. B. Begrambekov, S. V. Vergazov, A. A. Kuzmin, O. C. Fadina, and P. A. Shigin, J. Surf. Inverst. **4** (2010) 567.

[26] M. Balden and J. Roth, J. Nucl. Mater. **280** (2000) 39.

[27] P. Tamain, M. Kočan, J. Gunn, A. Kirk, J.-Y. Pascal, and M. Price, J. Nucl. Mater. **415** (2011) S1139.

[28] J. H. Cho, 2010, Structural Deformations of Carbon Nanotubes by Plasma Particle Interaction, Ph. D, Thesis, SNU

[29] J. F. Ziegler, J. P. Biersack, and U. Litttmark: The Stopping and Range of Ions in Solid. Oxford: Pergamon; 1985.

[30] https://kstar.nfri.re.kr/kstarweb.

[31] Y. S. Lim, S.H. Chi and K.Y. Cho, J. Nucl. Mater. **374** (2008) 123.

[32] A. N. Jones, G. N. Hall, M. Joyce, A. Hodgkins, K. Wen, T. J. Marrow, and B. J. Marsden, J. Nucl. Mater. **381** (2008) 152.

[33] Y. -J. Lee, J. Nucl. Mater. **325** (2004) 174.

[34] P. Roubin, C. Martin, C. Arnas, Ph. Colomban, B. Pégourié, and C. Brosset, J. Nucl. Mater. **337-339** (2005) 990.

[35] A. C. Ferrari and J. Robertson, Phys. Rev. B **61** (2000) 14095.

[36] T. Meguro, A. Hida, M. Suzuki, Y. Koguchi, H. Takai, Y. Yamamoto, K. Maeda, and Y. Aoyagi, Appl. Phys. Lett. **79** (2001) 3866.

[37] J. Y. Huang, Nano Lett. **7** (2007) 2335.

[38] Sun-Taek Lim, Jung-Hyun Cho, Sung-Ryul Huh, Goo-Hwan Jeong, and Gon-Ho Kim, Carbon **48** (2010) 3864.

[39] M. Meyyappan, Lance Delzeit, Alan Cassell, and David Hash, Plasma Sources Sci. Technol., **12** (2003) 205.

[40] L. B. Begrambekov, A. M. Zakharov, V. G. Telkovsky, Nucl. Instrum. Methods Phys. Res. B, **115** (1996) 456.

[41] J. B. Malherbe, CRC Crit. Rev. Solid State Mater. Sci., **19** (1994) 129.

[42] W. Möller, Appl. Phys. A, **56** (1993) 527.

[43] R. Janev, D. Reiter, and U. Samm: Collision Processes in Low-Temperature Hydrogen Plasmas, Report **JUEL-4105** (2003).

[44] I. B. Denysenko, S. Xu, J. D. Long, P. P. Rutkevych, N. A. Azarenkov and K. Ostrikov, J. Appl. Phys., **95** (2004) 2713.

[45] D. K. Davies, L. E. Kline, and W. E. Bies, J. Appl. Phys., **65** (1989) 3311.

[46] M. Hayashi: Nonequilibrium Processes in Partially Ionized Gases, New York: Plenum; 1990.

[47] W. L. Fite and R. T. Brackmann, Phys. Rev., **112** (1958) 1151.

[48] T. Nakano, H. Toyoda, and H. Sugai, Jpn. J. Appl. Phys., **30** (1991) 2912.

[49] Y.-K. Kim and M. Eugene Rudd, Phys. Rev. A, **50** (1994) 3954.

[50] A. G. Engelhardt and A. V. Phelps, Phys. Rev., **131** (1963) 2115.

[51] D. A. Alman, D. N. Ruzic, and J. N. Brooks, Phys. Plasmas, **7** (2000) 1421.

[52] S. F. Yoon, K. H. Tan, Rusli, and J. Ahn, J. Appl. Phys., **91** (2002) 40.

[53] V. Ivanov, O. Proshina, T. Rakhimova, A. Rakhimov, D. Herrebout, and A. Bogaerts, J. Appl. Phys., **91** (2002) 6296.

[54] M. Heintze, M. Magureanu, and M. Kettlitz, J. Appl. Phys., **92** (2002) 7022.

[55] K. Tachibana, M. Nishida, H. Harima, and Y. Urano, J. Phys. D, **17** (1984) 1727.

[56] D. Herrebout, A. Bogaerts, M. Yan, R. Gijbels, W. Goedheer,

and E. Dekempeneer, J. Appl. Phys., **90** (2001) 570.
[57] R. L. Mills, P. C. Ray, B. Dhandapani, R. M. Mayo, and J. He, J. Appl. Phys., **92** (2002) 7008.
[58] H. Chatham, D. Hils, R. Robertson, and A. C. Gallagher, J. Chem. Phys., **79** (1983) 1301.
[59] B. Szapiro, J. J. Rocca and T. Prabhuram, Appl. Phys. Lett., **53** (1988) 358.

초 록

중수소 플라즈마를 대면하는 흑연의 형상 변형이 탄수 불순물 생성량 증가에 미치는 영향에 대한 이해를 기반으로, 탄소 불순물 유입에 의한 중수소 플라즈마의 공간적 및 시간적 특성 변동을 연구하였다. 본 연구는 중수소 플라즈마 – 흑연 표면 상호작용 분석뿐 아니라 일반적인 플라즈마 – 표면 상호작용 해석에도 표면 형상을 고려하는 새로운 관점을 제시하고자 하였다. 중수소 플라즈마 – 흑연 표면 상호작용을 해석할 때 흑연 형상과 플라즈마 특성 변동 모두를 고려하는 것이 중수소 플라즈마 – 흑연 표면 상호작용 분석을 위해 필수적임을 밝혀내었다. 전자 사이클로트론 공명 플라즈마 실험 장치를 이용하여 주된 반응 영역이 흑연에 한정되고 타겟으로 이온이 수직 입사하도록 하였다. 1 – 3.5 × 10^{11} cm^{-3} 의 전자밀도, 3.5 – 5.5 eV 의 전자온도, 17 – 100 eV 의 이온 에너지를 갖는 조건에서 실험을 수행하였으며, 이 조건은 중수소 플라즈마와 흑연 벽면을 가지는 KSTAR scrape-off layer (SOL) 플라즈마에 유사한 조건이다.

중수소 플라즈마에 의한 흑연의 형상 변형을 플라즈마의 물리적 인자들인 이온 에너지, 이온속, 조사 시간을 하나로 묶은 개념인 에너지 조사량, 다시 말해서 단위 면적당 흑연에 전달된 총 에너지를 인자로 활용하여 해석을 수행하였다. 흑연의 형상 변형을 야기하는 탄소 원자가 이동하기 위해 필요한 에너지가 에너지 조사량에 비례할 것이므로, 에너지 조사량은 흑연의 형상 변형 정도를 결정한다. 또한 고에너지 중수소 이온이 탄소와 반응하고 결합을 형성하여, 흑

연 표면에 C-D 결합을 형성한다. 이를 통해 중수소 플라즈마와 흑연 벽면을 사용하는 KSTAR SOL 플라즈마의 정상 상태 조건까지의 흑연 형상 변형 추세를 분석하였다. 에너지 조사량 증가에 따라 흑연 표면의 형상이 평면에서 원뿔팁으로 진행함을 관측하였고, 원뿔 형상의 크기가 커지는 동시에 원뿔팁의 종횡비가 커지면서 뾰족한 원뿔팁이 형성되는 것을 관측하였다. 이온 입사에 의해 흑연 내부에 증가된 sp^3 구조의 일부가 나노 다이아몬드를 함유하여 주변 흑연 원자들과의 스퍼터링율의 차이로 원뿔팁이 형성될 수 있음을 밝혀내었다. 원뿔팁들이 3.8×10^5 V/m 이상의 쉬스 전기장 내에 있을 때 원뿔 형상의 다발로 성장함을 관측하였고, 이는 플라즈마의 물리적 특성인 에너지 조사량 및 쉬스 전기장과 함께 플라즈마의 화학 반응에 의한 탄소-중수소 결합의 형성이 원뿔 형상의 다발을 형성하는 메커니즘임을 밝혀내었다. 이로부터 흑연의 형상 변형을 분석할 때 플라즈마 물리 및 화학 반응 기반 해석의 필요성을 제시하였다.

원뿔 형상을 갖는 흑연에 대한 스퍼터링율 모델을 수립하였고, 이는 기존 Roth의 평면에 대한 스퍼터링율 모델과 비교하여 형상 변형에 의한 이온 입사각 증가와 후방산란된 이온의 추가적인 입사를 고려하는 특징을 갖는다. 이온 에너지 증가에 따른 흑연의 형상 변형은 평면을 고려한 모델에 대비해서 물리적 및 화학적 스퍼터링율이 증가함을 분석하였다. 이로부터 실험적으로 측정된 스퍼터링율이 평면에 대한 스퍼터링율 예측값보다 최대 2 배까지 큰 현상이 흑연의 형상 변형으로부터 야기함을 밝혀내었다. 이로부터 입사하는 플라즈마에 대한 해석이 흑연의 형상 변형 뿐 아니라 탄소 불순물 유입량 분석을 위해 필요함을 제시하였다.

탄소 불순물이 유입됨에 따라 공간 내 중수소 플라즈마의 전자 온도가 감소하고 전자 밀도가 증가하는 현상을 관측하였다. 이는 유입된 탄화중수소가 주 방전 기체인 중수소에 비해 전자와의 충돌에 의해 분해되거나 이온화될 확률이 높기 때문에 나타나는 현상임을 분석하였다. 공간 평균된 플라즈마 특성을 계산할 수 있는 글로벌 모델을 사용하여 탄소 불순물 유입에 의한 플라즈마의 공간 특성 변동을 실험적 진단값과 함께 분석하였다. 스퍼터링율의 증가가 중수소 플라즈마 내 탄화중수소 분자들을 수 % 정도까지 증가시킬 것이고, 탄소 불순물의 유입이 이러한 중수소 플라즈마 변동을 야기하는 인자임을 분석하였다. 이로부터 플라즈마의 특성 변동을 해석할 때 반응부산물의 유입 특성과 유입된 반응부산물과 플라즈마의 상호작용을 해석해야 하는 필요성을 제시하였다.

탄소 불순물이 유입됨에 따라 시간에 따라 중수소 플라즈마의 전자 온도가 감소하고 전자 밀도가 증가하는 현상을 관측하였다. 이는 운전 시간에 따른 흑연의 형상 변형이 스퍼터링율을 증가시켜서 야기된 현상임을 분석하였다. 즉, 이온 에너지와 이온속이 높아지는 경우인 에너지 조사량이 큰 경우에 흑연의 형상 변형이 더 크게 나타나고 이것이 더 큰 플라즈마 변동을 야기함을 분석하였다. 또한 중수소 플라즈마로의 탄소 불순물 유입에 의하여 운전 시간에 따라 증가하는 이온속이 후방산란된 이온의 추가적인 입사를 야기하여 스퍼터링율이 재증가하는 메커니즘을 밝혀내었다. 즉, 탄소 불순물 유입으로부터 야기된 플라즈마 변동이 벽면 침식률을 더 가속화시킬 수 있음을 예측할 수 있었다.

본 연구는 중수소 플라즈마와 흑연의 상호작용을 해석할 때 플라즈마와 흑연의 연구를 함께 수행해야 하며, 특히 흑연의 형상 변형

을 주요 인자로써 고려해야 함을 밝혀내었다. 플라즈마를 대면하는 흑연의 형상 변형이 플라즈마로의 탄소 불순물 유입량을 증가시켰고, 이것이 전자 온도 감소 및 전자 밀도 증가 현상을 심화시키는 것을 분석하였다. 이는 중수소 플라즈마와 흑연 대면재를 사용하는 KSTAR 또는 탄소와 수소를 포함하는 공정 플라즈마에서의 플라즈마 - 표면 상호 작용 자체에 대한 이해에 적용될 것이다. 또한 반응부산물이 플라즈마 특성에 영향을 미치는 것을 분석함으로써, 시간에 따른 플라즈마 특성 변동의 원인이 반응부산물에 의해 기인할 수 있음을 판단할 수 있는 기반을 제시하였다. 이를 기반으로 플라즈마 특성에 대한 예측, 더 나아가 플라즈마 특성을 제어하는 것에 기여할 것으로 기대된다.

주요어 : 중수소 플라즈마 - 흑연 표면 상호작용, 흑연 형상 변형, 스퍼터링율, 탄소 불순물 유입, 플라즈마 특성 변동

학번 : 2010-30257